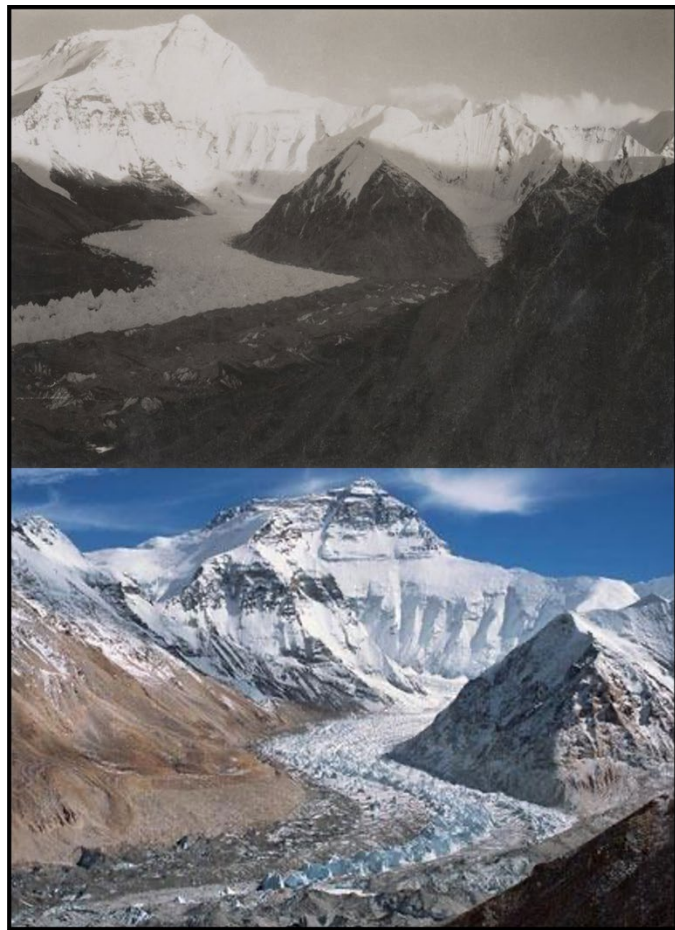


**Quantifying changes to debris thickness and extent on Rongbuk Glacier, Tibet, between 2000 and 2021, using an energy balance model, spectral imagery, and climate reanalysis data**



*“Like the huge waves of a brown angry sea”*

– George Mallory in Macfarlane (2008, p. 12)

**Part II Undergraduate Dissertation**

**Department of Geography**

**University of Cambridge**

**April 2025**

## Statement

I declare that this dissertation is my own unaided work, except for the assistance described in the *Acknowledgements*. I received 4.25 hours of supervision from my dissertation supervisor, Dr Rebecca Dell, including 1.25 hours at Part IB and 3 hours at Part II. I also received 1 hour of supervision from Professor Ian Willis at Part II, making my total supervision time across Parts IB and II 5.25 hours.

In addition, I received 1 hour of technical support from Dr Rebecca Dell on acquiring remote images from Google Earth Engine and 1 hour of technical support from Professor Neil Arnold to resolve technical issues with calculating slopes from digital elevation models.

Since its proposal, this dissertation's title has changed from "Monitoring changes to debris thickness and extent on the Rongbuk Glacier, Tibet, between 1999 – 2022, using an energy balance model, spectral imagery, and climate reanalysis data", to better reflect the temporal availability of data and this study's aims.

At 9,984 words, this dissertation is not less than 8,000 words and does not exceed 10,000 words.

## Acknowledgements

I am very grateful to those who have helped me with my dissertation.

Thank you to Dr Rebecca Dell for her advice as my dissertation supervisor and for technical support on acquiring images using Google Earth Engine; Professor Ian Willis for his advice and supervision; and Professor Neil Arnold for his technical support and for providing the MATLAB code to correctly calculate slopes from a digital elevation model.

I would also like to thank Dr David Rounce (Carnegie Mellon University) for sharing the MATLAB code for the surface energy balance model. I am grateful to the Royal Geographical Society (with IBG) for providing access to archival photos of George Mallory's 1921 Everest exhibition. Finally, I would like to thank my Director of Studies for their continued support throughout my undergraduate studies.

To my college geographers, thank you for your encouragement and companionship over the past three years; it's been wonderful.

To my family and friends, thank you for being there always and for putting up with my unwavering talk about debris-covered glaciers.

*Cover photos: Rongbuk Glacier with Mount Everest in the background in 1921 (George Mallory, © RGS-IBG) and 2007 (David Breashears).*

## Abstract

The evolution of debris cover on debris-covered glaciers is poorly constrained in projections of glacier retreat and melt. Under climate warming, debris cover is projected to expand up-glacier and form at a faster rate. Of particular interest is debris' initial emergence below the equilibrium line, where clean ice transitions into debris-covered ice. Debris cover has a non-linear effect on ice melt and accelerates ice melt in these transition areas. Producing a time series of debris evolution permits a better understanding of the transition of a glacier surface from clean ice to debris-covered ice.

This study produces a time series of debris cover evolution on Rongbuk Glacier, Tibet, between 2000 and 2021 using a surface temperature inversion energy balance model, Landsat 7 thermal imagery, and ERA-5 climate reanalysis data. Using established methods of quantifying changes in thickness and extent (Stewart et al., 2021), over the study period, Rongbuk Glacier's debris-covered area increased in size at a rate of 0.70 percentage points per year. The glacier-wide mean thickness rose from  $0.14 \pm 0.05$  m to  $0.21 \pm 0.06$  m.

This study further introduces two novel methods of monitoring debris cover evolution beyond simply analysing the evolution of individual distributed debris thickness maps, which are hampered by variability between maps in the time series. First, it stacks and averages distributed debris thickness maps over 5-year periods. Second, it uses pixel-wise linear regression to define a mean distributed 'debris accumulation rate' over the study period. It finds that debris is accumulating in the upper ablation area of Rongbuk Glacier at a rate of  $1.3 \pm 0.4$  mm yr<sup>-1</sup>. Debris accumulation in the accumulation zone at the base of mountainsides provides compelling evidence that the delivery of debris from adjacent mountainsides has increased.

This study also finds multiple limitations with energy balance modelling in the upper ablation area and suggests areas for further research. Methods of incorporating fractional debris cover within low-resolution satellite-obtained imagery are needed to better understand and predict the future evolution of debris cover, which would result in better estimates of glacier longevity under climate change.

## List of Contents

Statement .....	i
Acknowledgements.....	i
Abstract.....	ii
List of Contents.....	iii
List of Figures.....	v
List of Tables .....	vii
List of Abbreviations .....	vii
1    Introduction.....	1
1.1    Context.....	1
1.2    Supraglacial debris cover.....	2
1.2.1    Local effects of debris cover.....	2
1.2.2    Evolution of debris cover.....	4
1.2.3    Influence of supraglacial debris on glacier dynamics.....	5
1.2.4    Deriving supraglacial debris thickness .....	6
1.3    Study Site.....	9
1.4    Aims and Objectives.....	11
2    Data acquisition and preprocessing .....	13
2.1    Remotely sensed data .....	13
2.1.1    Surface temperature .....	13
2.1.2    Digital elevation model.....	13
2.2    ERA-5 reanalysis data .....	14
3    Methods .....	15
3.1    Energy balance model.....	18
3.2    Model uncertainty .....	20
3.3    A note on uncertainty propagation.....	21
3.4    Significant debris thickness changes .....	22

3.5	Debris accumulation rate .....	23
3.6	Stacked debris thickness estimates .....	23
3.7	Flux boxes.....	23
4	Results.....	25
4.1	Annual debris thickness and extent estimates .....	25
4.2	Estimated debris thickness change .....	27
4.3	Estimated debris accumulation rate.....	32
4.4	Stacked distributed debris thickness maps .....	33
5	Discussion.....	36
5.1	Down-glacier debris distribution .....	36
5.2	Study comparison .....	37
5.3	The use of temporal trends in the debris evolution workflow .....	38
5.4	Model-specific limitations and areas for future research .....	40
6	Conclusions.....	44
7	References.....	45
8	Appendices .....	55
8.1	Appendix 1 - Landsat 7 ETM+ image codes .....	55
8.2	Appendix 2 - ERA-5 data .....	57
8.3	Appendix 3 –Effective geographical sample size.....	58
8.4	Appendix 4 – Distributed debris thickness maps .....	59
8.5	Appendix 5 – Stacked and averaged distributed debris thickness maps .....	62

## List of Figures

<b>Figure 1.1.</b> Examples of Østrem Curves empirically derived from four glaciers. Note (a) showing the effective thickness and (b) the thickness at which debris-covered ice displays the same mean daily ablation as a climatologically equivalent clean-ice surface for Isfjallsglaciaren, Sweden. Figure adapted from Nicholson and Benn (2006, p. 463), which is adapted from Mattson et al. (1993, p. 292).....	3
<b>Figure 1.2.</b> Maps showing (A) the outline of Rongbuk Glacier, with the West Rongbuk Glacier (WRG), Middle Rongbuk Glacier (MRG), and the West-Middle Rongbuk Glacier tongue (WMRG); (B) estimated distributed debris thickness on Rongbuk Glacier from Rounce et al. (2021) – the ‘transition zone’ where current debris estimates are omitted is shown in the green square; and (C) estimated surface velocity of Rongbuk Glacier from Gardner et al. (2020). Glacier outlines are from the Randolph Glacier Inventory 7.0 (Pfeffer et al., 2014; RGI Consortium, 2023). The background image is from Landsat 8 (16/08/2022), courtesy of the U.S. Geological Survey.....	9
<b>Figure 1.3.</b> Photographs of Rongbuk Glacier facing south toward Mount Everest, showing the expansion of debris cover between (A) 1921 (George Mallory, © RGS-IBG) and (B) 2007 (David Breashears). MRG: Middle Rongbuk Glacier, WRG: West Rongbuk Glacier, WMRG: West-Middle Rongbuk Glacier. ....	10
<b>Figure 3.1.</b> Workflow for deriving individual distributed debris thickness maps (top) and significant debris thickness changes (bottom). Adapted from Stewart et al. (2021, p. 371).....	16
<b>Figure 3.2.</b> Workflow for calculating stacked and averaged distributed debris thickness maps (top) and distributed debris accumulation rates (bottom).....	17
<b>Figure 3.3.</b> 500 m flux boxes drawn along the MRG and tongue and WRG. The background image is from Landsat 8 (16/08/2022), courtesy of the U.S. Geological Survey .....	24
<b>Figure 4.1.</b> Flux-box-mean debris thicknesses for the Middle Rongbuk Glacier for each distributed debris thickness map between 2000 and 2021. Figure in the same style as Stewart et al. (2021, p. 378).....	26
<b>Figure 4.2.</b> A different method of visually conveying flux-box-meanned debris thicknesses for each distributed debris thickness map between 2000 and 2021, where each map is distinct rather than being overlaid. Note that the x-axis is not consistently distributed in time.....	26
<b>Figure 4.3.</b> Estimated evolution of the debris-covered fraction of Rongbuk Glacier between 2000 and 2021.....	27
<b>Figure 4.4.</b> Flux-box-averaged debris thicknesses and debris-covered fraction over Rongbuk Glacier. A and B show 2000, C and D show 2021. The debris-covered fraction is only shown	

from 5.5 km due to the glacier being close to 100% debris-covered on the tongue. The shaded area represents the uncertainty interval for the mean debris thickness. ....	29
<b>Figure 4.5.</b> Significant changes in debris thickness on Rongbuk Glacier between 2000 and 2021. Grey pixels represent debris which displayed no significant change in thickness. Note that the colour bar is asymmetrical around 0 because the thinning on the lake was significantly more than the highest thickness increase.....	30
<b>Figure 4.6.</b> Visual evidence of debris thickness change between 2000 and 2021. Rows represent the two years being compared. A) the reduction in debris cover due to the expansion of the supraglacial lake. B) Expansion of medial moraine and the thickening of dirty ice and the glacier margins. C) Thinning of debris along the glacier margin. D) Thickening of debris at the base of the headwall of Mount Everest. Pixels with an insignificant change in debris cover are shown in grey. Note that the colour bar is asymmetrical around 0 because the thinning on the lake was significantly more than the highest thickness increase. Visual images are from Landsat 7 (12/09/2000 and 04/07/2021) - courtesy of the U.S. Geological Survey.....	31
<b>Figure 4.7.</b> Estimates of the debris accumulation rate ( $\text{m yr}^{-1}$ ) across Rongbuk Glacier. ....	33
<b>Figure 4.8.</b> 5-year stacked and averaged distributed debris thickness maps for the transition zone. Grey pixels represent clean ice. ....	34
<b>Figure 4.9.</b> Present-day distributed debris thicknesses for Rongbuk Glacier. ....	35
<b>Figure 5.1.</b> Top: distributed debris thickness estimates for Rongbuk Glacier from this study, Rounce et al. (2021), and McCarthy et al. (2022). Bottom: Comparison maps between this study and Rounce et al.'s (2021) and McCarthy et al.'s (2022) estimates for distributed debris thicknesses over Rongbuk Glacier. All model estimates were resampled to match the pixel alignment of this study's model outputs before differencing. ....	37
<b>Figure 5.2.</b> Debris accumulation rates ( $\text{m yr}^{-1}$ ) at the base of the steep headwall of Mount Everest. 100 m contour lines are shown to emphasise the relief. Mount Everest's peak, at 8,848 m is shown in the bottom right. Debris can be clearly seen accumulating at the base of the headwall. Thinning higher up is indicative of the redistribution of debris on the headwall. ....	40
<b>Figure 5.3.</b> Explanations for why debris is observed to be below 273.15 K in certain pixels. Each option presents a single pixel and speculation for what its sub-pixel level composition may be. 42	
<b>Figure 5.4.</b> Image showing the reality of debris cover on Rongbuk Glacier's transition zone. Debris is discontinuous, which is not implied from the model outputs. Image from China Daily (2023). The location of the photo in relation to Rongbuk Glacier is shown in the top right.....	43

## List of Tables

<b>Table 1.1.</b> Mass Balance estimates (m w.e. yr <sup>-1</sup> ) for the Rongbuk Catchment over various periods, calculated from DEM differencing. ....	10
<b>Table 2.1.</b> Input meteorological variables for the Rounce and McKinney (2014) model and the respective ERA-5 reanalysis variables required for their derivation.....	15
<b>Table 3.1.</b> Variables and constants used in the RM14 model, alongside their values and units. ..	20
<b>Table 3.2.</b> Monte Carlo range for debris and meteorological properties for input into the Rounce and McKinney (2014) model. Ranges are taken from (Stewart et al., 2021). ....	21

## List of Abbreviations

DAIM	Sub-debris ablation inversion model
DAR	Debris accumulation rate
DCG	Debris-covered glacier
DDTM	Distributed debris thickness map
DEM	Digital Elevation Model
EBM	Energy balance model
ESS	Effective geographical sample size
GLOF	Glacier lake outburst flood
HMA	High Mountain Asia
m w.e.	Metres water equivalent
M22	McCarthy et al.'s (2022) distributed debris thickness for Rongbuk Glacier
MC	Monte Carlo
MRG	Middle Rongbuk Glacier
p.p.	Percentage points
R21	Rounce et al.'s (2021) distributed debris thickness for Rongbuk Glacier
RG	Rongbuk Glacier
RM14	Rounce and McKinney (2014) (specifically, their energy balance model)
STIM	Surface temperature inversion model
TZ	Transition Zone
WMRG	West-Middle Rongbuk Glacier tongue
WRG	West Rongbuk Glacier

# 1 Introduction

## 1.1 Context

Glaciers are a clear indicator of climate change, with their varied responses having significant social and environmental impacts (Huss et al., 2017). In High Mountain Asia (HMA), glaciers are losing mass at an accelerating rate in response to anthropogenically induced climate change (Marzeion et al., 2014; Maurer et al., 2019; Zemp et al., 2019; Shean et al., 2020), which is occurring disproportionately faster in HMA (Kraaijenbrink et al., 2017; Lalande et al., 2021). Mass loss in HMA is predicted to continue under all future Representative Concentration Pathways, with an estimated mass reduction of  $36 \pm 6\%$  by the end of the century (EOC) with a global temperature rise of  $1.5^{\circ}\text{C}$  (Kraaijenbrink et al., 2017). Understanding glaciers' future evolution under climate change is crucial for assessing their potential future contributions to eustatic sea level rise (Zhao et al., 2016; Edwards et al., 2021) and their longevity as sources of freshwater for 2 billion people (Immerzeel et al., 2010, 2020; Biemans et al., 2019; Farinotti et al., 2019). In the short term, meltwater discharge is projected to increase before declining once 'peak melt' has been surpassed (Immerzeel et al., 2010). Concurrently, mass loss also promotes the formation of supra- or proglacial lakes, dammed by debris and moraine, which present a risk of glacier lake outburst floods (GLOFs) to downstream communities (Zheng et al., 2021). Predicting future glacier behaviour is, therefore, crucial for both long-term water management and risk mitigation.

A key challenge in predicting future glacier behaviour and dynamics is accounting for the effects of supraglacial debris cover on debris-covered glaciers (DCGs), which modifies surface ablation (e.g., Reid and Brock, 2010) and remains poorly constrained in its extent, thickness, and future evolution (Herreid and Pellicciotti, 2020). Hitherto, debris cover is generally excluded from global-scale glacier models due to its sparse global distribution (Hock et al., 2019). Indeed, only 4.4-7.3% of extra-polar glacier areas are debris-covered, although this is spatially variable (Scherler et al., 2018; Herreid and Pellicciotti, 2020). Glaciers in HMA are 13% debris-covered, which increases to 36% in the Everest Region of Nepal (Kääb et al., 2012; Thakuri et al., 2014). Therefore, despite comprising a small proportion of the global glacierised area, it is paramount that debris cover is considered in future assessments of glacier evolution (Scherler et al., 2011). However, several unknowns hamper its inclusion, namely its spatial distribution, thickness, and temporal evolution (Herreid and Pellicciotti, 2020), which are critical for understanding its influence on glacier dynamics.

## 1.2 Supraglacial debris cover

Unravelling the evolution of debris cover and its influence on glacier dynamics presents a challenge due to their inherently reciprocal relationship. To address this, this section first examines the local-scale effects of debris cover on ice melt before exploring how debris evolves across the glacier surface over time. These insights are then used to assess the broader implications of debris cover for glacier-scale dynamics.

### 1.2.1 Local effects of debris cover

The primary influence of debris on glacier dynamics is its modification to the surface energy balance via its lower albedo to clean ice and its attenuation of the energy transfer from the atmosphere to the ice surface (e.g., Østrem, 1959; Brock et al., 2010). This results in a non-linear relationship between debris thickness and melt. Under thin debris, the lower albedo of debris dominates, exacerbating melt rates. Peak melt rates typically occur at a debris thickness of c.2 cm, the ‘effective thickness’ (Østrem, 1959; Mattson et al., 1993; Kayastha et al., 2000). The important distinction is that the peak melt under the effective thickness is greater than that of a climatologically equivalent clean-ice surface (Evatt et al., 2015). Beyond the effective thickness, the attenuation of radiation from the atmosphere through the debris negates the increased energy absorption at the surface by the darker debris, resulting in debris insulating the ice surface (Nicholson and Benn, 2013). This reduces a glacier’s sensitivity to external fluctuations in temperature and delays the delivery of maximum radiation receipt at the debris surface to the ice-debris interface, resulting in a lag time between peak receipt and peak sub-debris melt (Nicholson and Benn, 2013; Fyffe et al., 2014, 2019).

This non-linear relationship is captured by the Østrem Curve (Figure 1.1) (Østrem, 1959), which shows the empirical relationship between sub-debris melt and debris thickness and features a distinct rising limb up to a turning point at the effective thickness, followed by a logarithmic decline in the melt (Nicholson and Benn, 2006). The Østrem Curve’s rising limb is likely a result of thin debris cover being sparsely distributed rather than a continuous layer of uniform thickness (Adhikary et al., 1997, 2000; Reid and Brock, 2010; Fyffe et al., 2020). Thus, the surface albedo is a function of the ratio between debris-covered and clean-ice surfaces, and the turning point occurs near the point where debris cover becomes continuous (Nicholson and Benn, 2006). Wind at the ice-debris interface may also play a role in the distinct shape of the Østrem Curve (Evatt et al., 2015). The initial debris build-up reduces the wind speed at the ice-debris interface, reducing evaporation rates. Subsequently, latent heat previously used in evaporation becomes available for melting, exacerbating melt. Upon the debris reaching a sufficient thickness, the effective

thickness, the wind speed at the ice-debris interface becomes insignificant, allowing insulation to take precedence (Evatt et al., 2015). The exact value of the effective thickness varies per glacier, dependent on the debris' properties, such as the albedo and effective thermal conductivity, which vary in time and space due to variations in the debris' lithology and water content (Hinkel, 1997; Nicholson and Benn, 2013).

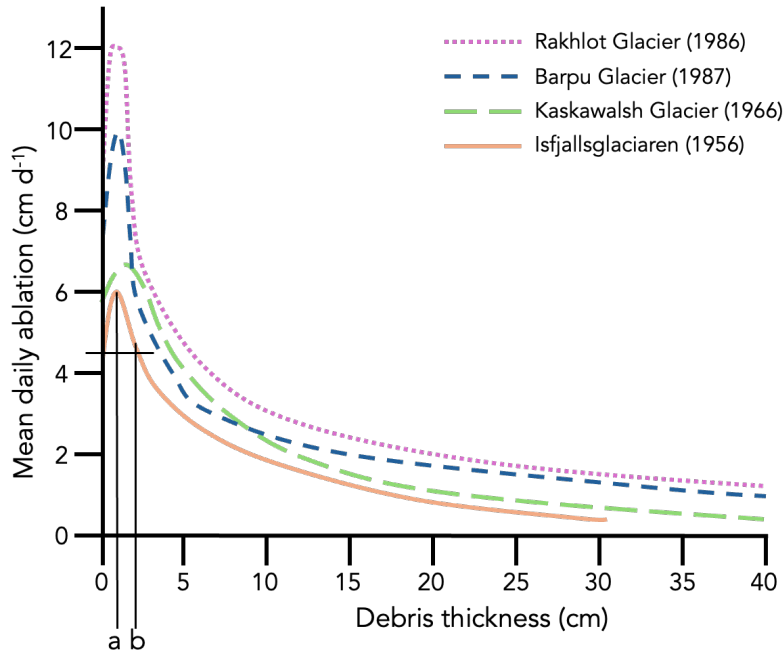


**Figure 1.1.** Examples of Østrem Curves empirically derived from four glaciers. Note (a) showing the effective thickness and (b) the thickness at which debris-covered ice displays the same mean daily ablation as a climatologically equivalent clean-ice surface for Isfjallsglaciaren, Sweden. Figure adapted from Nicholson and Benn (2006, p. 463), which is adapted from Mattson et al. (1993, p. 292).

### 1.2.2 Evolution of debris cover

Debris is delivered onto glacier surfaces through avalanching and landslides from adjacent mountainsides (Benn and Owen, 2002). In the accumulation zone, deposited debris is buried by snow and is typically advected down-glacier englacially (Anderson and Anderson, 2018; Scherler et al., 2018). Upon reaching the ablation zone, debris cover tends to emerge through englacial meltout, aided by vertical ice displacement (Benn and Owen, 2002; Benn et al., 2012; Anderson and Anderson, 2016, 2018). Debris is largely unaffected during englacial transport (Boulton, 1978), therefore, the primary distribution of emerging debris is governed by the glaciological controls depositing debris up-glacier (Kirkbride and Deline, 2013). Empirical studies (e.g., Goodsell et al., 2005) have found that englacial debris is concentrated in debris-rich septa, formed

from medial moraine when glacier tributaries coalesce (Gibson et al., 2017). Therefore, debris tends to initially emerge as transverse bands, which results in local minimums in sub-debris ablation, causing moraine relief to increase down-glacier relative to adjacent clean ice (Kirkbride and Deline, 2013). Gravitational processes then redistribute debris locally down slopes, modifying the primary pattern and widening medial moraines, resulting in continuous debris cover (Anderson, 2000; Kirkbride and Deline, 2013). Since the glacier is also moving during the formation of continuous debris cover, continuous debris cover does not occur immediately at the equilibrium line altitude (ELA) but rather below it (Shea et al., 2021). Therefore, there is a region of discontinuous debris-covered ice, ‘dirty ice’, which exists between clean ice and continuously debris-covered ice (Fyffe et al., 2020). The greater the glacier velocity, the greater the size of the dirty ice region (Shea et al., 2021). These regions are of particular interest because dirty ice is situated within the Østrem Curve’s rising limb, exacerbating ablation, and, therefore, they display the highest ablation rates over a glacier (Reid and Brock, 2010; Fyffe et al., 2014; Evatt et al., 2015). As debris thickens as debris meltout occurs, the ablation rate is then reduced.

The thickness of debris cover increases when the glacier’s capacity to remove debris is less than the accumulation rate (Kirkbride and Deline, 2013). This balance is strongly related to glacier velocity. Glacier velocities typically decline monotonically toward the terminus, resulting in more debris accumulating than being evacuated at each point along the glacier (Anderson and Anderson, 2018). This causes an increase in debris thickness down-glacier, which is characteristic of most DCGs globally (Anderson and Anderson, 2018; Rounce et al., 2021). Secondary processes such as gravitational redistribution, fluvial erosion, the opening of crevasses, or further supply of debris from avalanches and landslides modify this general trend, resulting in highly localised variability in debris thickness, which modify debris-covered surfaces into a highly hummocky topography (Reznichenko et al., 2011; Anderson and Anderson, 2016; Bartlett et al., 2021). Indeed, debris thickness can vary by several meters over horizontal distances of a few decimetres (Nicholson and Benn, 2013; Nicholson and Mertes, 2017).

In the context of climate change, the processes governing debris emergence and redistribution are becoming increasingly significant. Rising ELAs increase the spatial extent of debris meltout, thereby increasing the debris-covered area and debris’ spatial influence on glacier dynamics (Thakuri et al., 2014; Rowan et al., 2015; Shea et al., 2021). Therefore, understanding how the distribution of supraglacial debris evolves is important for understanding debris’ role in future glacier dynamics. This currently remains a challenge, and debris evolution is presently omitted in regional estimates of glacier longevity (Kraaijenbrink et al., 2017; Fyffe et al., 2020)

### 1.2.3 Influence of supraglacial debris on glacier dynamics

The insulation effect of thick debris allows DCGs to advance into much lower elevations than typically possible for clean-ice glaciers (Anderson, 2000; Benn et al., 2012). Because of the heterogeneous distribution of supraglacial debris across a glacier (Section 1.2.2) and debris' effect on ablation (Section 1.2.1), sub-debris ablation is highly varied spatially, resulting in DCGs displaying different hydrological characteristics to their clean-ice counterparts.

The increase in debris thickness down-glacier results in an inverse ablation gradient up-glacier in the ablation area (Rounce et al., 2021). Therefore, DCGs typically have their highest ablation in the upper ablation area toward the equilibrium line (Reid and Brock, 2010; Fyffe et al., 2014; Evatt et al., 2015; Rounce et al., 2021), which causes the topographic profile of debris-covered glacier tongues to flatten. Flattening reduces driving stresses and flow velocities, which results in stagnation and mass loss primarily through surface lowering rather than retreat (Hambrey et al., 2008; Quincey et al., 2009), which makes quantifying retreat a poor indicator of glacier health (Scherler et al., 2011).

The low gradient of debris-covered tongues, coupled with their hummocky terrain, results in supraglacial meltwater streams having highly sinuous profiles (Benn et al., 2017; Miles et al., 2019). Hummocky terrain is also conducive to the formation of supraglacial ponds in local topographic minimums, which exacerbate local melt rates through their lower albedo and by revealing and undercutting their surrounding ice cliffs (Miles et al., 2020). The exposure of ice at low elevations results in localised regions of high melt, which can be up to an order of magnitude higher than the surrounding debris-covered ice (Immerzeel et al., 2014; Brun et al., 2018). Over time, multiple supraglacial ponds can coalesce to form large supraglacial lakes when runoff is dammed by debris or terminal moraine (Benn et al., 2012). Their formation presents a hazard because the collapse of debris and moraine dams can result in GLOFs (Benn et al., 2012). 697 GLOFs have been documented between 1833 and 2022 in HMA, resulting in 6906 fatalities and damage to downstream infrastructure (Shrestha et al., 2023). Thus, monitoring of DCGs is crucial for mitigating the risks of GLOFs and improving our understanding of DCG dynamics, which are strongly influenced by the distribution and thickness of supraglacial debris.

### 1.2.4 Deriving supraglacial debris thickness

Field-based measurements of supraglacial debris thickness provide high-accuracy point measurements. However, they are labour-intensive and often require traversing hazardous glacier terrain. Furthermore, they are unable to capture spatial or temporal variability at scale and are typically confined to the glacier tongue (Aubry-Wake et al., 2023; Fontrodona-Bach et al., 2025).

Consequently, remote sensing methods are key to quantifying debris thickness. While no remote sensing method can directly monitor debris thickness, inverse modelling can be used, where debris thickness is inferred using a different measurable physical quantity whose variation is somewhat governed by debris thickness. The two most common variables used are surface temperature and surface lowering, which have been related to debris thickness through both empirical and physics-based approaches (e.g., Mihalcea et al., 2008b; Rounce and McKinney, 2014). Each inverse problem is complex because debris is not the sole factor influencing each measured quantity. For example, surface temperatures are influenced by meteorological conditions, and surface lowering can be indicative of both melt and dynamic thinning.

#### **1.2.4.1 Empirical relationships**

Various empirical relationships between surface temperature and debris thickness have been proposed, comprising different linear and exponential relationships (e.g., Mihalcea et al., 2008b, 2008a; Boxall et al., 2021). The optimal relationship is glacier-specific, and empirical models rely heavily on the availability of well-distributed data representative of the full range of debris thicknesses and surface temperatures, limiting their performance and transferability spatially and temporally (Schauwecker et al., 2015; Boxall et al., 2021). Physics-based models have been developed to improve upon these limitations.

#### **1.2.4.2 Physics-based models**

Two main types of physics-based models have been used to estimate debris thickness: surface temperature inversion (STIMs) and sub-debris ablation inversion models (DAIMs).

STIMs combine surface temperature measurements with a surface energy balance of the glacier at an instantaneous point in time, where debris thickness is the only unknown (e.g., Foster et al., 2012; Rounce and McKinney, 2014; Schauwecker et al., 2015). These models use the observed debris surface temperature to infer debris thickness based on a modelled temperature gradient through the debris to the debris-ice interface. Section 3.1 provides a detailed description of the surface energy balance model (EBM).

STIMs are beneficial because they enable debris thickness to be estimated from any single surface temperature map, given the availability of meteorological data at the time of surface temperature acquisition. Furthermore, it is computationally inexpensive and, therefore, suitable for this study. Stewart et al. (2021) use a surface temperature inversion approach to develop a time series of distributed debris thickness maps (DDTMs) on three well-studied glaciers using ERA-5 reanalysis data as a meteorological input. They find that this approach is suitable for detecting the early emergence of debris within dirty ice zones. However, they express caution on using a limited

number of DDTMs to estimate changes due to localised and time-specific variability, which affects individual debris thickness estimates. Thus, trends using multiple DDTMs are instead recommended. Owing to estimating debris thickness at an instantaneous point in time, STIMs must make estimates of the energy balance at the debris surface and the temperature gradient through the debris, which is highly non-linear and is controlled not only by present meteorological and debris properties but also past properties (Schauwecker et al., 2015). Accounting for the debris' history to derive a more realistic estimate of the energy balance and debris temperature gradient is possible using dynamic EBMs (e.g., Reid and Brock, 2010), which use meteorological data to derive a better estimate of the surface energy balance and temperature gradient (McCarthy, 2019). However, these approaches are much more computationally expensive.

STIMs are also limited to deriving debris thicknesses up to 0.5 m (Foster et al., 2012), limiting their ability to estimate the total volume and mass of debris cover. Beyond 0.5 m, the debris' surface temperature becomes significantly less sensitive to debris thickness, and estimates are inaccurate (Foster et al., 2012). However, the impact on estimated sub-debris ablation rates is less significant because it approaches a minimum towards this thickness (Rounce and McKinney, 2014).

Conversely, DAIMs (e.g., Ragettli et al., 2015; Rounce et al., 2018; McCarthy et al., 2022) are, to the author's knowledge, the only models which can accurately derive debris thicknesses beyond 0.5 m. DAIMs first estimate the sub-debris ablation rate, assumed to be equal to the annual climatic mass balance, because debris is located in the ablation area (Rounce et al., 2015). The climatic mass balance is calculated using the rate of surface lowering, ice thickness, and surface velocity. Debris thickness is then iteratively increased using a Monte Carlo (MC) framework within an EBM until the modelled sub-debris melt is equivalent to the previously derived estimate (Rounce et al., 2015, 2018). A key assumption of DAIMs is that debris thickness and its spatial distribution remain constant over the modelled period. This assumption restricts their application to near-stagnant glacier zones, where observed surface lowering can be attributed solely to ablation (Rounce et al., 2018). In dynamic regions, such as portions of Rongbuk Glacier, changes to the glacier surface are a function of not only ablation but also surface movement and vertical displacement, which violates the above assumption. Later studies (e.g., Westoby et al., 2020) have been able to employ the inverse sub-debris ablation model by correcting digital elevation models (DEMs) for surface movement and vertical displacement prior to differencing them, allowing ablation-caused surface lowering to be isolated. However, this correction was largely necessitated by their use of high-resolution unmanned aerial vehicle (UAV) data rather than satellite imagery.

Rounce et al. (2021) use a DAIM to derive the first estimates of globally distributed debris thickness. They do not correct for surface displacement, thereby restricting their application of the DAIM to near-stagnant regions (Rounce et al., 2021). Non-stagnant regions' debris thicknesses are estimated by using a surface-temperature-inversion approach, calibrated using the surface temperature and derived estimates of the highest elevation stagnant region (Rounce et al., 2021).

Both model types have further limitations to their application. Surface temperatures derived from satellites typically have a 60-100 m resolution. Debris cover can vary significantly within this scale (Section 1.2.2), and multiple features, including ice cliffs and supraglacial ponds, may exist within a single pixel. This 'mixed pixel' effect reduces the surface temperature in debris-covered pixels by exposing bare ice, resulting in underestimations of debris thicknesses (Rounce et al., 2018). Further limitations stem from poorly constrained debris properties (e.g., surface roughness, albedo, and thermal conductivity). Properties are usually derived from local measurements over other glaciers and are assumed to be constant over space and time, which may not accurately represent local conditions (Reid and Brock, 2010; Rounce and McKinney, 2014). More accurate estimates require site-specific measurements (Velasco et al., 2024). Nevertheless, sensitivity testing using MC simulations can determine the impact of previously derived physical properties on thickness estimates and quantify uncertainty (Rounce and McKinney, 2014).

Given the limitations of DAIMs in dynamic glacier regions and the absence of corrected surface lowering data for Rongbuk Glacier, this study adopts a STIM to quantifying changes to debris thickness and extent. The following section outlines the glaciological setting of Rongbuk Glacier.

### 1.3 Study Site

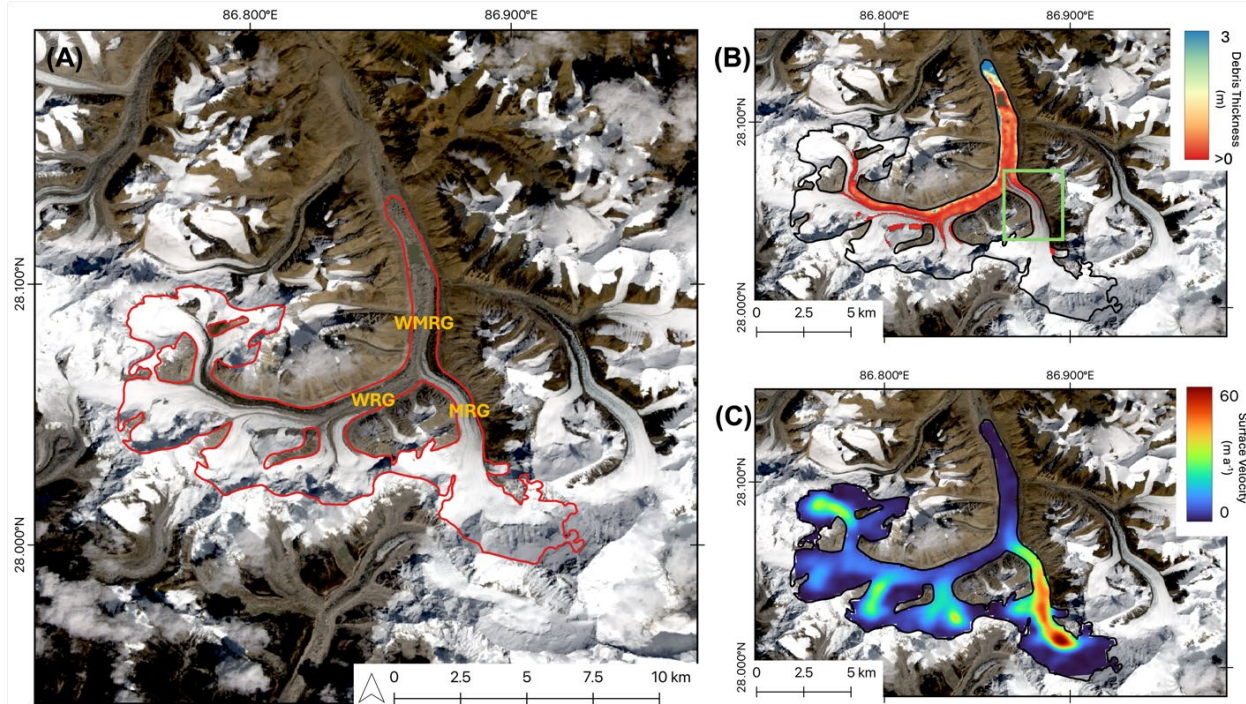


**Figure 1.2.** Maps showing (A) the outline of Rongbuk Glacier, with the West Rongbuk Glacier (WRG), Middle Rongbuk Glacier (MRG), and the West-Middle Rongbuk Glacier tongue (WMRG); (B) estimated distributed debris thickness on Rongbuk Glacier from Rounce et al. (2021) – the ‘transition zone’ where current debris estimates are omitted is shown in the green square; and (C) estimated surface velocity of Rongbuk Glacier from Gardner et al. (2020). Glacier outlines are from the Randolph Glacier Inventory 7.0 (Pfeffer et al., 2014; RGI Consortium, 2023). The background image is from Landsat 8 (16/08/2022), courtesy of the U.S. Geological Survey.

Rongbuk Glacier (RG) ( $28.05^{\circ}\text{N}$ ,  $86.86^{\circ}\text{E}$ ) lies between altitudes of 5120 and 8848 m and has three primary tributaries: the East RG, which has detached from the main tongue; the Middle RG, which flows from Mount Everest’s north face; and the West RG. The latter two converge to form the stagnant West-Middle Rongbuk Tongue (WMRG), which is debris-covered (See Figure 1.2A) (Quincey et al., 2009; Ye et al., 2015, 2022).

RG is in negative mass balance (Ye et al., 2015, 2022; Li et al., 2018). Table 1.1 shows mass balance estimates for RG. Despite a general trend toward negative mass balance, driven by increasing temperatures, RG displayed a short positive anomaly ( $0.11 \pm 0.15 \text{ m w.e. yr}^{-1}$ ) between 2012 and 2015 due to increased precipitation, albeit with limited certainty (Ye et al., 2022). Overall, increased melt and rising ELAs have likely resulted in enhanced debris melt out at higher elevations, advancing the debris-covered area up-glacier. This is confirmed through visual

satellite imagery, which shows the expansion of dirty ice and the widening of medial moraine (Figure 4.6). On a longer timescale, photos of RG taken in 1921 by George Mallory during the first British expeditions to climb Mount Everest (Gillman, 1993) present a stark contrast with the glacier today (Figure 1.3), showing a significant expansion in the debris-covered area, especially on the MRG.

Time Period	Glacier Mass Balance (m w.e. yr <sup>-1</sup> )	Reference
1974 - 2000	-0.21 ± 0.11	Ye et al. (2022)
1974 - 2021	-0.20 ± 0.03	Ye et al. (2022)
2000 - 2006	-0.41 ± 0.11	Ye et al. (2022)
2000 - 2012	-0.51 ± 0.05	Li et al. (2018)
2012 - 2015	0.11 ± 0.15	Ye et al. (2022)
2015 - 2021	-0.45 ± 0.11	Ye et al. (2022)

**Table 1.1.** Mass Balance estimates (m w.e. yr<sup>-1</sup>) for the Rongbuk Catchment over various periods, calculated from DEM differencing.

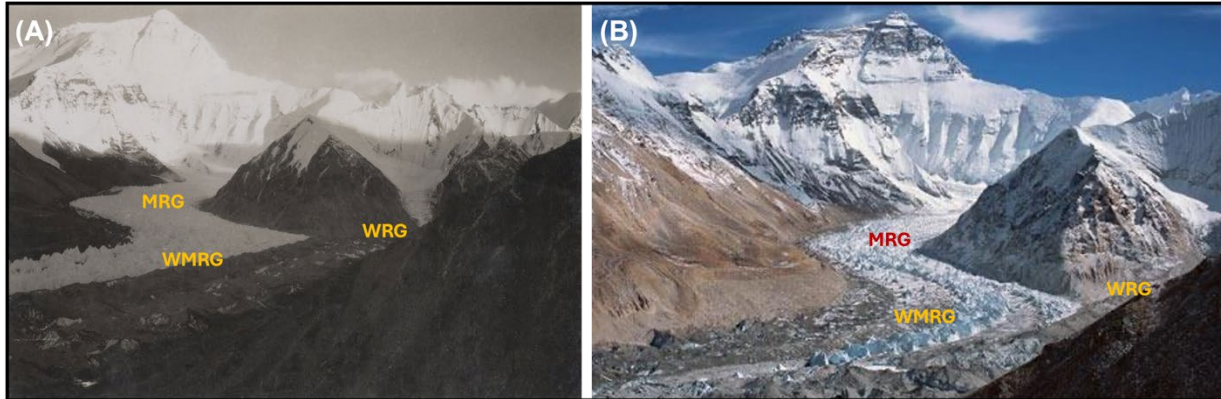


**Figure 1.3.** Photographs of Rongbuk Glacier facing south toward Mount Everest, showing the expansion of debris cover between (A) 1921 (George Mallory, © RGS-IBG) and (B) 2007 (David Breashears). MRG: Middle Rongbuk Glacier, WRG: West Rongbuk Glacier, WMRG: West-Middle Rongbuk Glacier.

The literature has given RG's debris cover considerably less attention than its southern counterpart, Khumbu Glacier, especially regarding its thickness. The influence of debris cover on RG is clear through the growth in the number and area of supraglacial lakes on its tongue, which has an almost linear topographic gradient of 1.9 degrees (Wessels et al., 2002; Quincey et al., 2009; Ye et al., 2009; Watson et al., 2016; Bartlett et al., 2021). RG is covered in 632,000 m<sup>2</sup> of

supraglacial lakes and ponds, of which its main supraglacial lake, located 2-3 km from its terminus, accounts for 410,000 m<sup>2</sup> (Watson et al., 2016). Thus, given debris' large role on RG's dynamics, it is important that its debris cover, and thickness are mapped.

Despite RG's prominent location on the north slope of Mount Everest, no previous study has specifically mapped the extent or thickness its debris cover. DDTMs have only been produced as part of global- or regional-scale estimates of debris distribution or thickness. To the author's knowledge, Rounce et al. (2021) and McCarthy et al. (2022) provide the only DDTMs, hereafter R21 and M22, respectively, of RG using physics-based models. M22 consistently underestimates debris thickness compared to R21, with no clear explanation except for their differing methods (McCarthy et al., 2022). Both estimates of debris thickness, which range from a few centimetres to several metres, fall in the range of *in situ* measurements conducted in 1959 (Shen, 1975; Ye et al., 2015).

Both studies also fail to quantify debris in the dirty ice areas, including medial moraine, particularly on the MRG (See Figure 1.2B), in what this study will hereafter refer to as the 'transition zone' (TZ). This omission could be because the MRG is moving at a faster rate (30-40 m yr<sup>-1</sup>, Gardner et al., 2022) than the threshold used by Rounce et al. (2021) to prescribe 'near-stagnant' areas (7.5 m yr<sup>-1</sup>). McCarthy et al. (2022) prescribe a minimum debris thickness of 0.02 m for detection, which could suggest their inability to detect debris within the TZ. It is important that debris thickness is quantified in the TZ due to it being more sensitive to changes in debris thickness because of sparse debris cover and its existence on the rising limb of the Østrem Curve (Fyffe et al., 2020). Not only should a single thickness estimate be made, but quantifying how its thickness is changing is essential for understanding the future evolution of debris cover.

## 1.4 Aims and Objectives

Section 1.2.2 has demonstrated that debris is expanding up-glacier, initially promoting dirty ice formation before continuous debris cover develops. Areas further up-glacier will typically exhibit higher flow velocities due to steeper relief at higher elevations. Therefore, dirty ice regions are unlikely to be accounted for in globally DDTMs, which are unable to resolve debris thickness in dynamic areas or exclude thin debris layers typical of dirty ice due to minimum detection thresholds (Sections 1.2.4.2 and 1.3). In these regions, glacier dynamics are more sensitive to emerging debris because dirty ice enhances ablation (Section 1.2.1). Therefore, there should be increased focus on these areas where clean ice is transitioning to debris-covered ice.

Section 1.3 has demonstrated that debris cover and thickness on RG has received little attention. Furthermore, the TZ has been omitted in current DDTMs, which use DAIMs, highlighting the TZ as a key example of an unrepresented dirty ice region. Due to the TZ's dynamic nature, it is likely that the debris distribution is evolving, therefore making it appropriate to develop a time series of debris evolution. DAIMs assume that debris extent and thickness remain constant over the modelled period (Section 1.2.4.2). This assumption limits their application to near-stagnant areas. This assumption is violated over the MRG, which is moving at 30-40 m yr<sup>-1</sup> (Gardner et al., 2022). Therefore, it is appropriate to employ a STIM where debris thickness can be quantified at a single point in time.

Given these findings, this study aims to quantify changes in supraglacial debris thickness and extent on RG, with a specific focus on the MRG and the evolution of the TZ. This aim is addressed by dividing it into smaller research objectives:

1. Acquire and preprocess relevant, freely available data over a sufficient time span for debris emergence to input into a physics-based model.
2. Apply a STIM from Rounce and McKinney (2014), hereafter the 'RM14 model', to derive a time series of DDTM estimates.
3. Use an MC framework to quantify uncertainty in thickness estimates.
4. Identify statistically significant debris thickness and extent changes using the uncertainty estimates derived in 3.
5. Introduce methods to analyse temporal trends in debris thickness to reduce the influence of time-specific variability in individual estimates.

## 2 Data acquisition and preprocessing

This section describes the acquisition and preprocessing of input data required for implementing the RM14 model. The key inputs are surface temperature data, meteorological data, elevation data, and debris properties (Rounce and McKinney, 2014).

### 2.1 Remotely sensed data

#### 2.1.1 Surface temperature

Landsat 7 Enhanced Thematic Mapper+, hereafter Landsat 7, surface temperature images (Band 6) were acquired of the study site between 1999 and 2022, the time span available on Google Earth Engine (Gorelick et al., 2017). Band 6 images have a spatial resolution of 60 x 60 m, automatically resampled to 30 x 30 m. Landsat 8 and 9's thermal bands have the same resampled resolution; however, they are derived from a 100 x 100 m resolution. Therefore, it was appropriate to use Landsat 7 surface temperature images to reduce the impact of the mixed pixel effect. Thus, the derived DDTMs have a resolution of 30 x 30 m. The surface temperature from Landsat 7 images has an uncertainty of  $\pm 1.0^{\circ}\text{C}$  (Coll et al., 2010)

Images were filtered to the ablation season (May-September), and images with cloud cover or extensive snowfall were discarded. Moreover, Landsat 7 images are affected by a 'striping effect' caused by a malfunction in its Scan Line Corrector in May 2003, leading to  $\sim 22\%$  data loss per image (Scaramuzza and Barsi, 2005). Images where  $>50\%$  of the study site was affected by striping were discarded. Hereafter, the glacier area unaffected by striping will be referred to as the 'applicable glacier area'.

36 images were appropriate for analysis, spanning 12/09/2000 to 04/07/2021 (Appendix 1).

#### 2.1.2 Digital elevation model

A DEM is required to distribute meteorological data spatially and correct longwave radiation for the topography. The ASTER Global-DEM (Abrams et al., 2010) was used as the DEM input for the model simulations. The ASTER Global-DEM has a spatial resolution of 30 x 30 m and was resampled using QGIS to match the pixel alignment of the Landsat 7 imagery. The ASTER Global-DEM has a vertical uncertainty of  $\pm 10$  m and a horizontal geolocation accuracy of  $<50$  m (Fujisada et al., 2005; Nuth and Kääb, 2011).

The RM14 model accounts for the topographic effects on incoming shortwave radiation, using each pixel's slope, aspect, and hillshade calculated from the DEM. Each was calculated for its

respective Landsat 7 image. A MATLAB script adapted from the RM14 was used to calculate the Sun's azimuth and elevation, relevant for calculating the hillshade.

## 2.2 ERA-5 reanalysis data

ERA-5 reanalysis data has a horizontal resolution of  $\sim 0.5^\circ \times 0.5^\circ$ , spanning 137 atmospheric pressure levels and the single (surface) level (C3S, 2017). Reanalysis-based estimates were acquired for the hour closest to the time of each Landsat 7 overpass ( $\sim 10:15$  am local time) at the single level (Hersbach et al., 2018). Table 2.1 shows the necessary meteorological inputs for the RM14 model and the necessary ERA-5 variables required for their derivation.

Reanalysis-based estimates were bilinearly interpolated to the study site ( $28.05^\circ\text{N}$ ,  $86.86^\circ\text{E}$ ) (Appendix 2). Bilinear interpolation to a single point on the glacier was appropriate because the RM14 model assumes that meteorological variables are uniform over the glacier or extrapolated over the glacier using simple assumptions (Rounce and McKinney, 2014).

RM14 Model Variables	ERA-5 Acquisition Variable
2 m Air Temperature (K)	2 m Air Temperature (K)
Incoming Shortwave Radiation ( $\text{W m}^{-2}$ )	Surface Solar Radiation Downwards ( $\text{W m}^{-2}$ )
Incoming Longwave Radiation ( $\text{W m}^{-2}$ )	Surface Thermal Radiation Downwards ( $\text{W m}^{-2}$ )
Relative (%) and Specific Humidity ( $\text{kg kg}^{-1}$ ) <sup>1</sup>	2 m Dew Point Temperature (K) 2 m Air Temperature (K) Surface Pressure (Pa)
Wind Speed ( $\text{m s}^{-1}$ )	10 m U Wind Component ( $\text{m s}^{-1}$ ) 10 m V Wind Component ( $\text{m s}^{-1}$ )

**Table 2.1.** Input meteorological variables for the Rounce and McKinney (2014) model and the respective ERA-5 reanalysis variables required for their derivation.

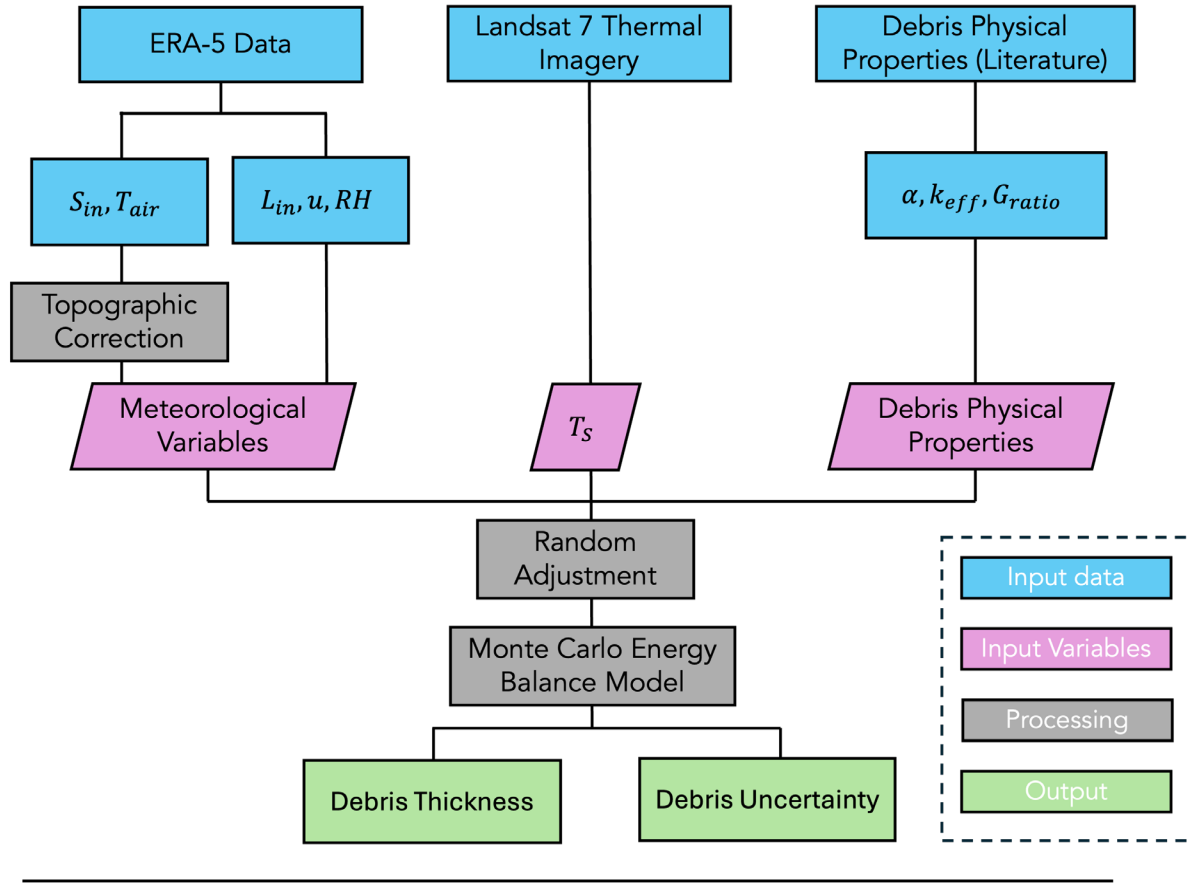
### 3 Methods

This study largely follows Stewart et al.’s (2021) workflow, where reanalysis-based estimations of meteorological data are used alongside remotely sensed surface temperature and elevation data as inputs into an EBM to solve for debris thickness. DDTMs are produced for each Landsat 7 acquisition using the RM14 model. Then, an MC framework is used to quantify uncertainty and identify pixels displaying a significant change in debris thickness over time. This study further builds on Stewart et al.’s (2021) workflow in two primary ways. First, it calculates the significant change in debris volume while accounting for uncertainty propagation and correlation. Second, it mitigates localised and time-specific variability, which affects individual DDTMs and, thus, their comparison (Stewart et al., 2021) by (i) defining a ‘debris accumulation rate’ (DAR), and (ii) stacking and averaging DDTMs. Figures 3.1 and 3.2 show the full method workflow.

---

<sup>1</sup> Relative and Specific humidity were derived using ERA-5 variables, however, despite being declared as variables in the RM14 model, they are never used for debris calculations because the RM14 model assumes there is no latent heat flux. They are included here for consistency with the model input arguments.

Debris thickness at  $T_x$ :



Difference between  $T_1$  and  $T_2$ :

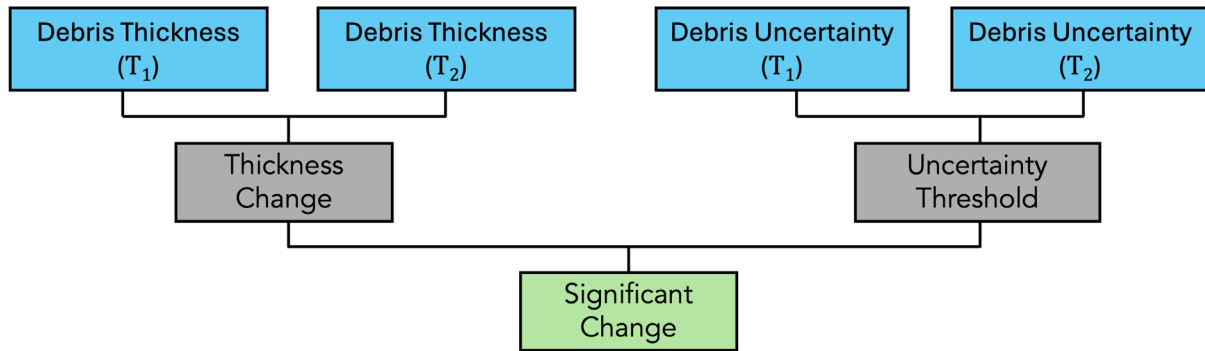


**Figure 3.1.** Workflow for deriving individual distributed debris thickness maps (top) and significant debris thickness changes (bottom). Adapted from Stewart et al. (2021, p. 371).

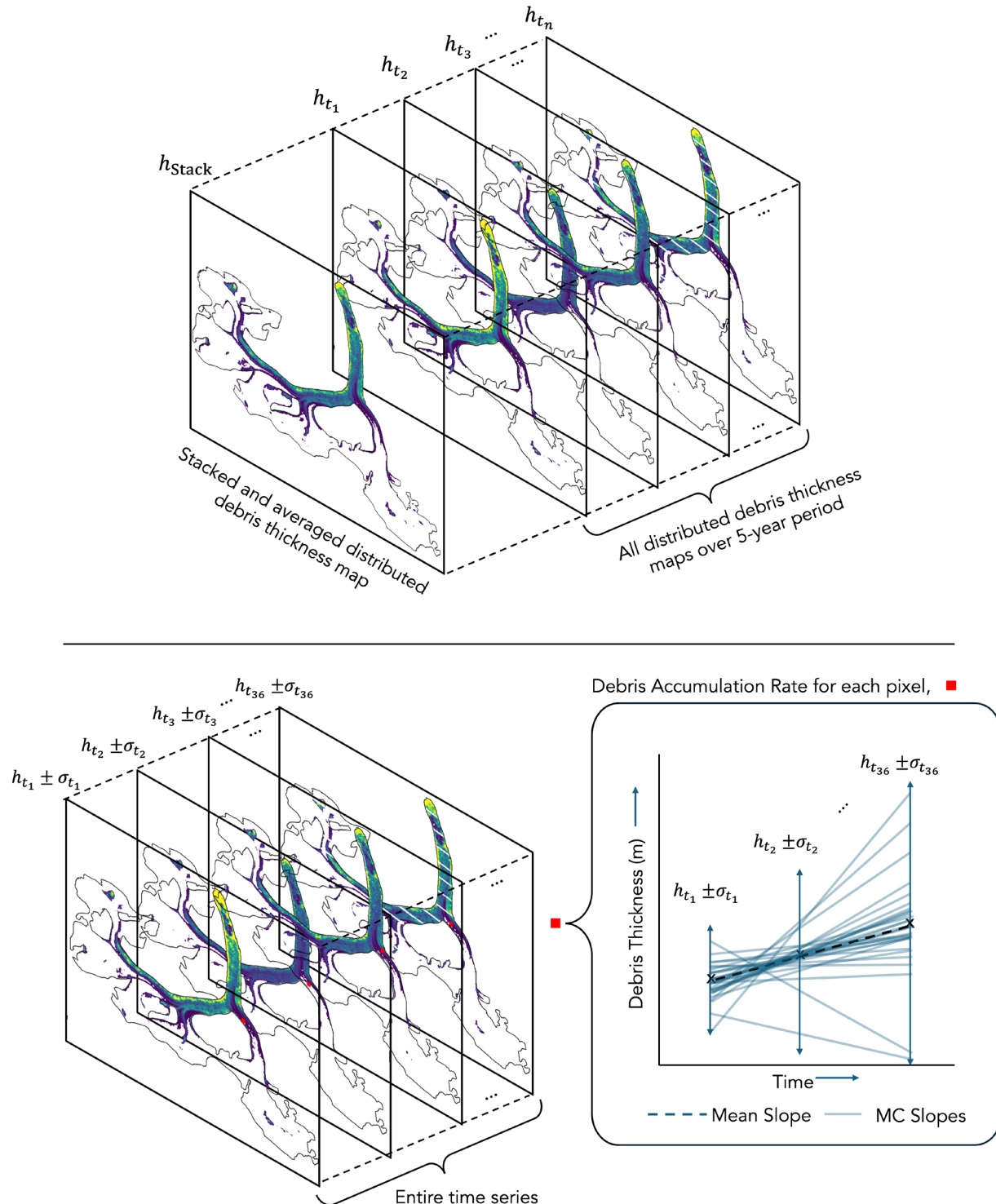


**Figure 3.2.** Workflow for calculating stacked and averaged distributed debris thickness maps (top) and distributed debris accumulation rates (bottom).

### 3.1 Energy balance model

This section outlines the RM14 model. DDTMs were generated for each Landsat 7 surface temperature map by solving for debris thickness for each pixel using the RM14 model. Table 3.1 shows values of constants and units. The energy balance at the debris surface is:

$$M = R_n + LE + H - Q_c, \quad (1)$$

where  $M$  is the energy available for melt,  $R_n$  is the net radiation flux,  $LE$  is the latent heat flux,  $H$  is the sensible heat flux, and  $Q_c$  is the ground heat. The RM14 model assumes a steady state, therefore,  $M$  is 0. Furthermore, the debris surface is assumed to be dry during the daytime in the ablation season under cloud-free conditions (Brock et al., 2007, 2010). Therefore,  $LE$  is assumed to be 0. (1) can thus be simplified to:

$$Q_c = R_n + H. \quad (2)$$

The received radiation,  $R_{in}$ , can be expressed as:

$$R_{in} = S_{in}(1 - \alpha) + \varepsilon L_{in}, \quad (3)$$

where  $S_{in}$  is incoming shortwave radiation,  $\alpha$  is the debris' albedo,  $\varepsilon$  is the debris' emissivity, and  $L_{in}$  is incoming longwave radiation. The albedo and emissivity are assumed to be uniform over the glacier surface (Nicholson and Benn, 2006; Rounce and McKinney, 2014).  $S_{in}$  was corrected for each pixel to account for the effects of topography (shading and aspect, calculated using the DEM) (Hock and Noetzli, 1997; Rounce and McKinney, 2014).  $L_{in}$  is assumed to be uniform across the glacier surface based on the diffuse nature of longwave radiation. The emitted longwave radiation,  $L_{out}$ , is derived by the Steffan-Boltzmann law, scaled by the debris' emissivity because debris is not a perfect black body:

$$L_{out} = \varepsilon \sigma T_s^4, \quad (4)$$

where  $\sigma$  is the Steffan-Boltzmann constant and  $T_s$  is the surface temperature. Therefore, by combining (3) and (4),  $R_n$  is expressed as:

$$R_n = S_{in}(1 - \alpha) + \varepsilon(L_{in} - \sigma T_s^4). \quad (5)$$

$H$  is:

$$H = \rho_{air} \left( \frac{P}{P_0} \right) cuA(T_{air} - T_s), \quad (6)$$

where  $\rho_{\text{air}}$  air's density,  $P$  is the atmospheric pressure,  $P_0$  is sea level atmospheric pressure,  $c$  is air's specific heat capacity,  $u$  is the wind speed,  $A$  is the dimensionless transfer coefficient, and  $T_{\text{air}}$  is the air temperature 2 m above the glacier surface. Air temperature in physics-based models is typically extrapolated vertically from station or reanalysis data using a spatially constant lapse rate (e.g., Rounce and McKinney, 2014). However, this may not hold for DCGs, where the use of constant lapse rates typically underestimates air temperatures in the daytime (Steiner and Pellicciotti, 2016). Air temperature above debris is strongly related to the surface temperature under strong insolation conditions in the morning, where the net longwave radiation and turbulent sensible heat fluxes are in the upward direction (Brock et al., 2010). Thus, the air temperature is more sensitive to surface temperature than elevation. This is especially relevant because Landsat 7 acquisitions are in the morning (~10:15 local time), and only cloud-free images are used as model inputs. Empirical relationships have been used to derive air temperature from surface temperature using *in situ* measurements on DCGs (e.g., Schauwecker et al., 2015). However, without sufficient distributed air and surface temperature data on RG, deriving a reliable empirical relationship between the two is not possible. Therefore, a spatially constant lapse rate was used.

$Q_c$  is:

$$Q_c = G_{\text{ratio}} \frac{k_{\text{eff}}(T_s - 273.15)}{h}, \quad (7)$$

where  $k_{\text{eff}}$  is the effective thermal conductivity of debris, and  $h$  is the debris thickness.  $G_{\text{ratio}}$  is the non-linear approximation factor introduced by Rounce and McKinney (2014), which accounts for the thermal gradient between the debris surface and debris-ice interface being non-linear. The debris-ice interface is assumed to be warmed to 273.15 K in the ablation season.

(2) and (5-7) can be used to solve for debris thickness because every other variable is known or can be derived.

RM14 model variable / constant	Symbol	Value	Unit	Value Citation
Energy available for melt	$M$	-	$\text{W m}^{-2}$	-
Net radiation flux	$R_n$	-	$\text{W m}^{-2}$	-
Latent heat flux	$LE$	-	$\text{W m}^{-2}$	-
Sensible heat flux	$H$	-	$\text{W m}^{-2}$	-
Ground heat flux	$Q_c$	-	$\text{W m}^{-2}$	-
Surface temperature	$T_s$	-	K	-
Air temperature	$T_{\text{air}}$	-	K	-
Atmospheric pressure	$P$	-	Pa	-
Wind speed	$u$	-	$\text{m s}^{-1}$	-
Albedo	$\alpha$	0.3	-	Nicholson and Benn (2006)
Emissivity	$\varepsilon$	0.95	-	Nicholson and Benn (2006)
Steffan-Boltzmann Constant	$\sigma$	$5.67 \times 10^{-8}$	$\text{W m}^{-2} \text{K}^{-4}$	-
Density of air	$\rho_{\text{air}}$	1.29	$\text{kg m}^{-3}$	-
Sea level atmospheric pressure	$P_0$	101,325	Pa	-
Specific heat capacity of air	$c$	1,010	$\text{J kg}^{-1} \text{K}^{-1}$	-
Environmental lapse rate		6.5	$\text{K km}^{-1}$	-
G <sub>ratio</sub>	$G_{\text{ratio}}$	2.7	-	Rounce and McKinney (2014)
Debris effective thermal conductivity	$k_{\text{eff}}$	0.95	$\text{W m}^{-1} \text{K}^{-1}$	Rounce and McKinney (2014)

**Table 3.1.** Variables and constants used in the RM14 model, alongside their values and units.

## 3.2 Model uncertainty

An MC framework was used to calculate the uncertainty in debris thickness for each model output. Meteorological data and debris properties were both varied randomly over a uniform

distribution between an appropriate interval over 1000 MC simulations for each debris thickness output (Table 3.2). It was appropriate to use the same ranges as Stewart et al. (2021) because their study of Khumbu Glacier is in a similar geographical setting. It was necessary to randomly vary both meteorological data and debris properties because although meteorological data and debris properties vary in space and time (Nicholson and Benn, 2013), the model assumes that meteorological data is constant over the entire glacier or extrapolated using simple temperature lapse rates and that debris properties remain constant over the glacier area and time (Stewart et al., 2021).

Subsequent estimated debris thicknesses are reported as the mean  $\pm$  the standard deviation of the MC runs.

<b>Debris / Meteorological Property</b>	<b>Value</b>	<b>Monte Carlo Range</b>
Albedo	0.3	0.1-0.4
Surface roughness (m)	0.02	0.0035-0.0600
Effective thermal conductivity ( $\text{W m}^{-1} \text{K}^{-1}$ )	0.96	0.47-1.62
Gratio	2.7	$\pm 0.4$
$T_s$ (K)	-	$\pm 1.0$
$T_{air}$ (K)	-	$\pm 4.0$
$u$ ( $\text{m s}^{-1}$ )	-	$\pm 1.0$
$S_{in}$ ( $\text{W m}^{-2}$ )	-	$\pm 10\%$
$L_{in}$ ( $\text{W m}^{-2}$ )	-	$\pm 10\%$

**Table 3.2.** Monte Carlo range for debris and meteorological properties for input into the Rounce and McKinney (2014) model. Ranges are taken from (Stewart et al., 2021).

### 3.3 A note on uncertainty propagation

This study's methods involve calculating results using values with uncertainty. Therefore, uncertainty propagation must be considered.

When temporal analysis was conducted, the uncertainties between different DDTMs were assumed to be independent and thus, added in quadrature (Taylor, 1997). This is appropriate because each DDTM is isolated in time, and its associated uncertainties are derived from different MC simulations (Taylor, 1997; Heuvelink, 1998).

When spatial analysis was conducted, spatial autocorrelation must be considered because the uncertainties within single DDTMs are likely to be correlated due to being derived from the same MC simulation(s). Indeed, the uncertainties show a highly significant, positive spatial autocorrelation (e.g., Moran's I value: 0.933,  $p < 0.01$  for the first DDTM), thereby violating the assumption of individual independence. Thus, the true uncertainty is likely to be higher than adding in quadrature because uncertainties are less likely to cancel (Taylor, 1997; Griffith, 2005; Lee, 2017). To account for this, the quadrature-sum was scaled using an effective geographical sample size (ESS) correction, where the ESS represents the equivalent number of independent observations needed to provide the same uncertainty as those that are correlated (Griffith, 2005; Grace, 2019). After cancelling like terms (Appendix 3), the quadrature-sum-derived uncertainty is adjusted by:

$$\sigma_{\text{Adj}} = \sigma \sqrt{\left(\frac{1+I}{1-I}\right)}, \quad (8)$$

where  $I$  is Moran's I value, calculated from a Moran's I test on the individual uncertainties (Grace, 2019).

### 3.4 Significant debris thickness changes

Estimated debris thickness changes were derived from differencing output DDTMs. Pixels affected by the striping effect in either or both compared DDTMs were excluded from further analysis.

The uncertainty in the debris thickness change for each pixel is the quadrature-sum (Stewart et al., 2021):

$$\sigma_{\Delta h} = \sqrt{\sigma_{t1}^2 + \sigma_{t2}^2}, \quad (9)$$

where  $\sigma_{t1}$  and  $\sigma_{t2}$  are the debris thickness uncertainties from the two DDTMs being compared. Pixels with an estimated debris thickness change greater than the uncertainty threshold were classed as having a significant debris thickness change. The remaining insignificant pixels were excluded from further analysis.

The total area of significant change was calculated by summing the surface area of each pixel. The model propagates no uncertainty for the debris-covered area because pixels are either debris-covered or not. Similarly, the total volume change was calculated by multiplying each pixel's thickness difference by its area and summing.

### 3.5 Debris accumulation rate

Pixel-wise linear regression was performed to estimate the average DAR over the study period for each pixel. An MC simulation was used to estimate the uncertainty in the DAR. Over 1000 iterations, the debris height for each map was randomly drawn from its respective distribution of debris thicknesses, obtained from the original MC simulations in Section 3.2. The mean and standard deviation of the 1000 slopes for each pixel were used as the estimated DAR and its associated uncertainty, respectively. The suitability of using a linear model is discussed in Section 5.3.

### 3.6 Stacked debris thickness estimates

Starting in 2000, DDTMs were stacked and averaged over five-year periods. Pixels affected by the striping effect were excluded from the mean calculation. Consequently, certain stacked pixels were derived using fewer stacked pixels than others.

### 3.7 Flux boxes

Following the methods of Rounce et al. (2018) and Stewart et al. (2021), ~500 m long contiguous ‘flux boxes’ were demarcated up to 12.5 km from the terminus over the MRG and tongue where debris was clearly present in a visual image from 2022 (Figure 3.3). Flux boxes were also demarcated to the same length on the WRG. Taking the mean debris thickness within each flux box provides a view of the up-glacier distribution of debris thickness.

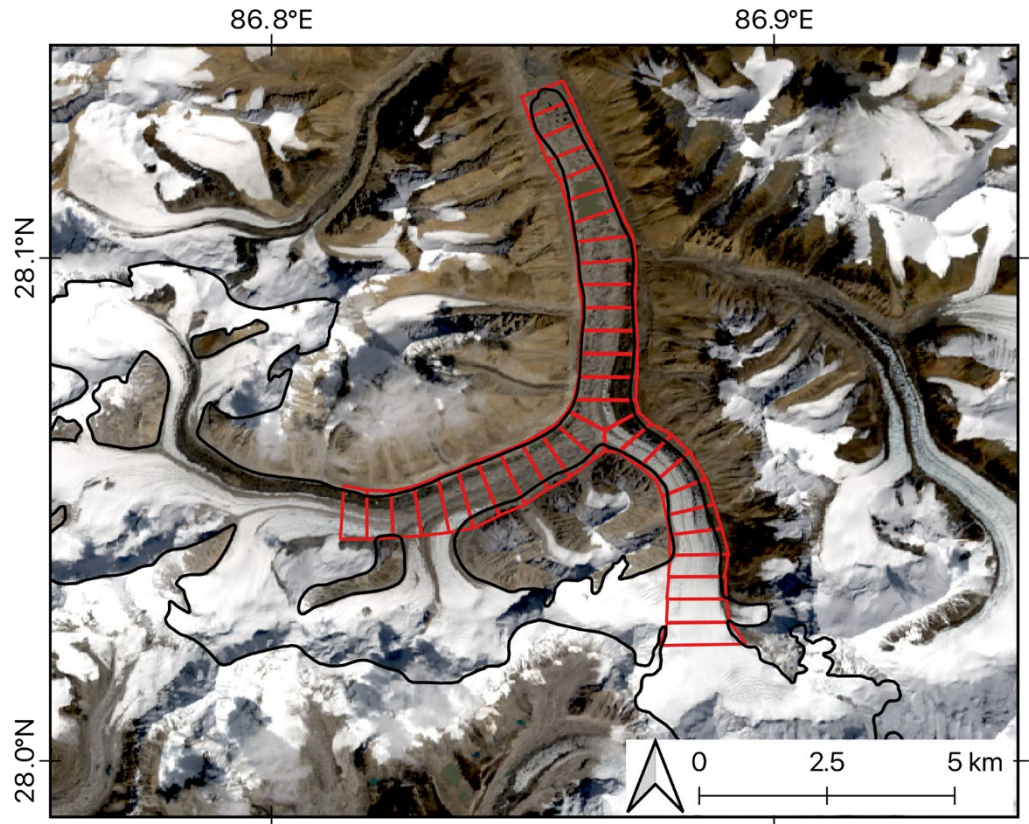


**Figure 3.3.** 500 m flux boxes drawn along the MRG and tongue and WRG. The background image is from Landsat 8 (16/08/2022), courtesy of the U.S. Geological Survey

## 4 Results

### 4.1 Annual debris thickness and extent estimates

DDTMs were computed for the ablation season of RG between 2000 and 2021, comprising 36 maps (Appendix 4). The glacier-wide mean debris thickness on RG fluctuates with no clear trend between 2000 and 2019, with a minimum mean debris thickness of  $0.065 \pm 0.03$  m on 28/07/2018 and a maximum mean debris thickness of  $0.18 \pm 0.07$  m on 02/09/2008. From 2019, the debris thickens over the entire glacier, rising to a maximum mean thickness of  $0.29 \pm 0.09$  m on 02/08/2020. Despite fluctuations in mean thickness, the spatial pattern remains generally consistent across DDTMs – debris is thickest at the terminus, with a sharp decline and then resurgence between 2-3 km from the terminus due to the supraglacial lake, followed by a decrease until 11 km. Between 11 and 12.5 km, there is a small resurgence in debris thickness, which is attributed to debris gathering at the base of a cliff, which then diminishes at 12.5 km. Figure 4.1 shows flux-box-meanned debris thicknesses along the MRG for all 36 DDTMs, similar to as in Stewart et al. (2021). However, distinguishing individual years is difficult. Figure 4.2 attempts to present a clearer perspective of debris evolution.

The applicable debris-covered proportion on RG increases between 2000 and 2021, rising from 28.1% to 42.9% (0.70 percentage points (p.p.)  $\text{yr}^{-1}$ ) due to the expansion of debris up-glacier from an elevation of 5,530 to 5,650 m ( $5.7 \text{ m yr}^{-1}$ ). Unlike the mean debris thickness, which fluctuates with no clear trend except for a strong increase from 2019 onwards, the applicable debris-covered proportion generally displays an increasing trend over the measurement period. In the TZ, the emergence of medial moraine can be seen, as well as the upwards movement of the debris-covered area. Despite the general trend, significant interannual variability is present. For example, the debris-covered areas for 28/07/2018 and 13/06/2019 are 14.8% and 16.0%, respectively, which are more than 10 percentage points lower than adjacent maps in the time series. Both maps only quantify debris thickness on the glacier tongue, where debris is known to be thick. They also produce the lowest mean thickness values across all flux-boxes and have glacier-wide mean debris thicknesses of  $0.065 \pm 0.03$  and  $0.062 \pm 0.04$  m, respectively. Inspection of visual imagery from each scene shows no extensive snowfall or reason for the RM14 model to fail to quantify debris. Therefore, this suggests that the RM14 model does not entirely capture the energy balance to correctly estimate debris (Section 5.4).

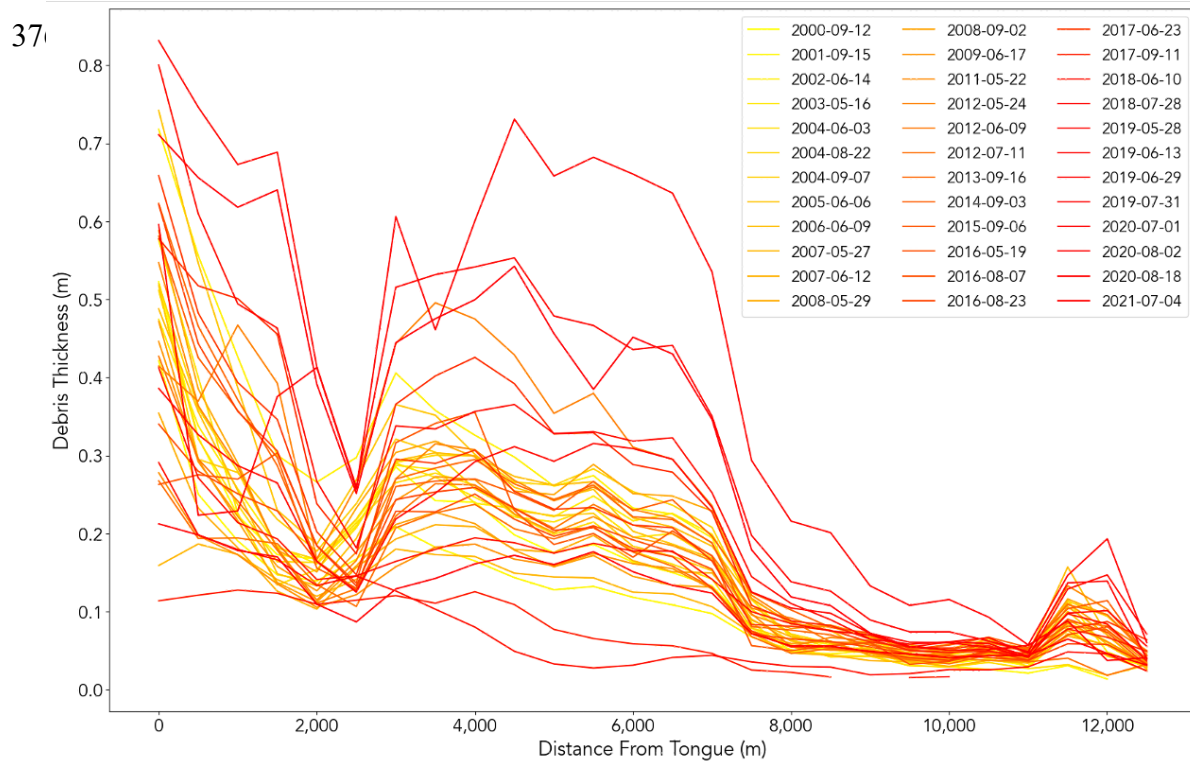


**Figure 4.1.** Flux-box-mean debris thicknesses for the Middle Rongbuk Glacier for each distributed debris thickness map between 2000 and 2021. Figure in the same style as Stewart et al. (2021, p. 378).

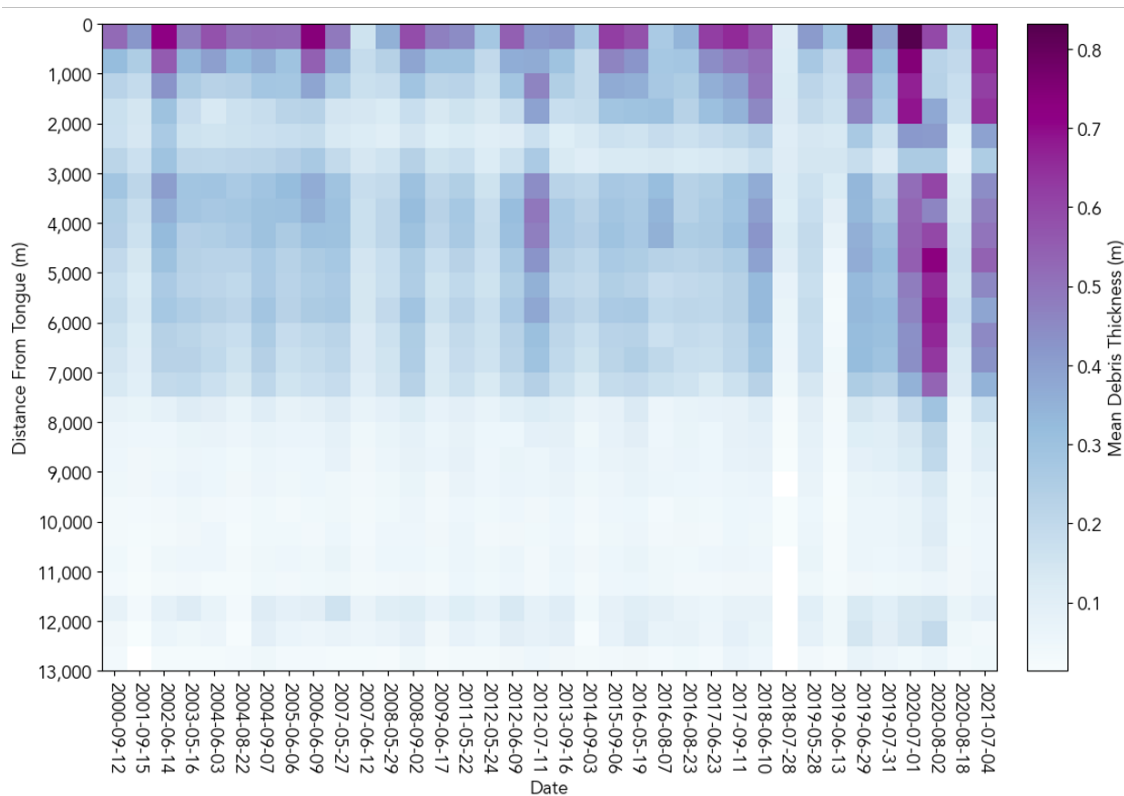


**Figure 4.2.** A different method of visually conveying flux-box-meanned debris thicknesses for each distributed debris thickness map between 2000 and 2021, where each map is distinct rather than being overlaid. Note that the x-axis is not consistently distributed in time.

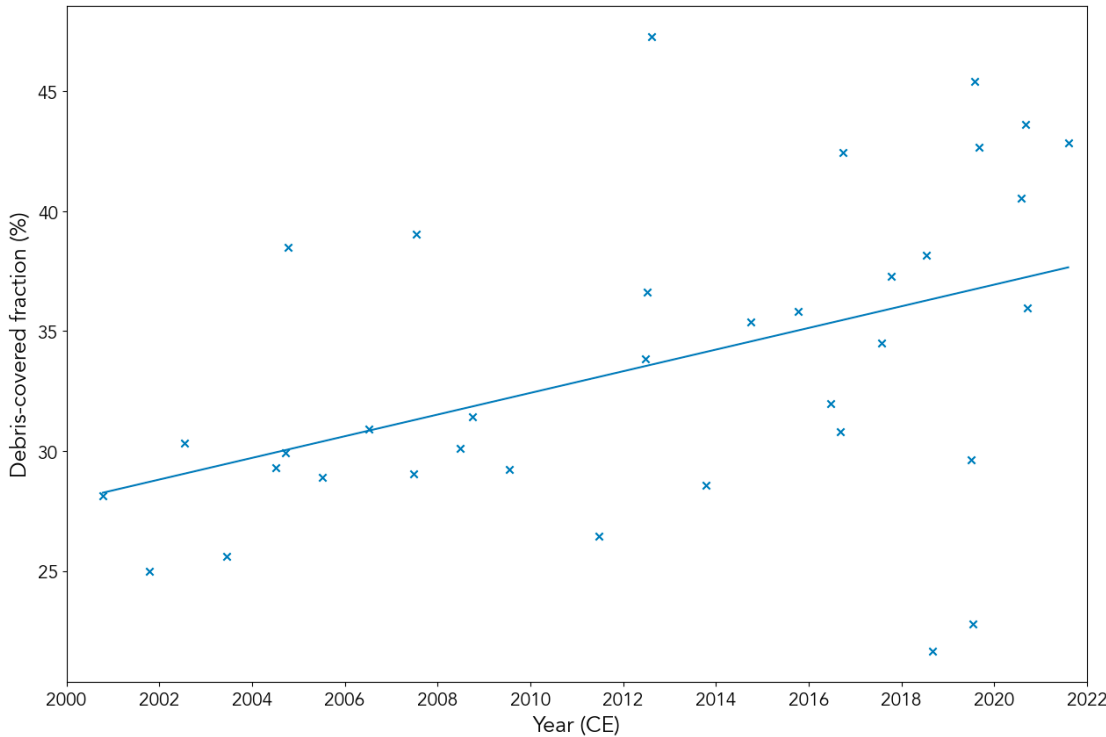


**Figure 4.3.** Estimated evolution of the debris-covered fraction of Rongbuk Glacier between 2000 and 2021.

## 4.2 Estimated debris thickness change

The debris thickness change between 2000 and 2021 was estimated by comparing the first and last DDTMs from the time series: 12/09/2000 and 04/07/2021. Flux-boxed averaged debris thicknesses for 2000 and 2021 are shown in Figure 4.4A and C. Across debris-covered areas, most of RG experienced an increase in debris thickness. The mean debris thickness increased from  $0.14 \pm 0.05$  m to  $0.21 \pm 0.06$  m over the study period.

Upon applying the uncertainty threshold to identify significant changes in debris thickness (Section 3.4),  $15.71 \text{ km}^2$  (16.43%) of the applicable glacier area displayed a significant change in debris thickness, of which  $14.91 \text{ km}^2$  was an increase (Figure 4.5). This area is mostly restricted to the upper ablation area, with  $10.38 \text{ km}^2$  (66% of the significant area) being originally clean ice in 2000. The expansion of the debris-covered area is clearly seen in the increase in the debris-covered portion of each flux box (Figure 4.4B and D). Areas with thicker debris have greater uncertainties from the RM14 model, due to the model's increased sensitivity to higher surface temperatures (Rounce and McKinney, 2014). Therefore, more substantial thickening is required in areas of thick debris for changes to be detected. Consequently, detected changes are biased toward areas of thinner debris cover.

Significant thickening is observed on medial moraines, dirty ice, and the glacier margins (Figure 4.6B), the base of the headwall of Mount Everest (Figure 4.6D). Significant thinning is observed

where the supraglacial lake has grown (Figure 4.6A) and, occasionally, on the glacier margins (Figure 4.6C). It is worth noting that the model is classifying water-covered pixels as debris-covered, which is a key limitation of the model, discussed further in Section 5.4. Using the debris thickness estimates and their respective errors, the area change corresponds to a debris-volume gain of  $434,000 \pm 20,000 \text{ m}^3$ .

Despite this seemingly significant result, clearly showing the thickening and expansion of debris up-glacier, this result does not appear to be robust. Different pairwise comparisons yield conflicting trends. For example, differencing the first map (12/09/2000) and the penultimate map (18/08/2021) shows a decline in the mean debris thickness from  $0.14 \pm 0.05 \text{ m}$  to  $0.098 \pm 0.004 \text{ m}$ . This result was expected, hence the usage of new methods.

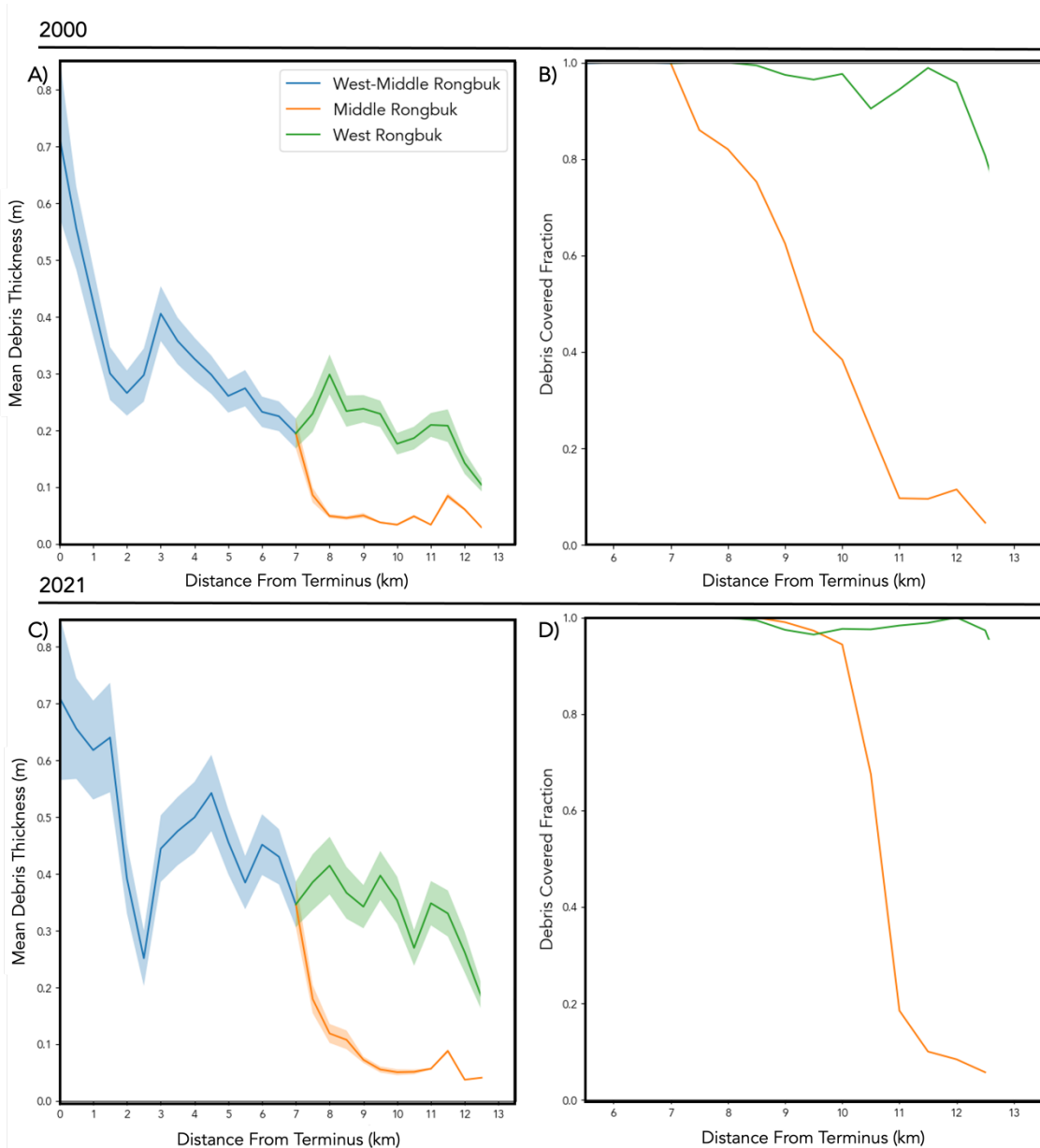


**Figure 4.4.** Flux-box-averaged debris thicknesses and debris-covered fraction over Rongbuk Glacier. A and B show 2000, C and D show 2021. The debris-covered fraction is only shown from 5.5 km due to the glacier being close to 100% debris-covered on the tongue. The shaded area represents the uncertainty interval for the mean debris thickness.

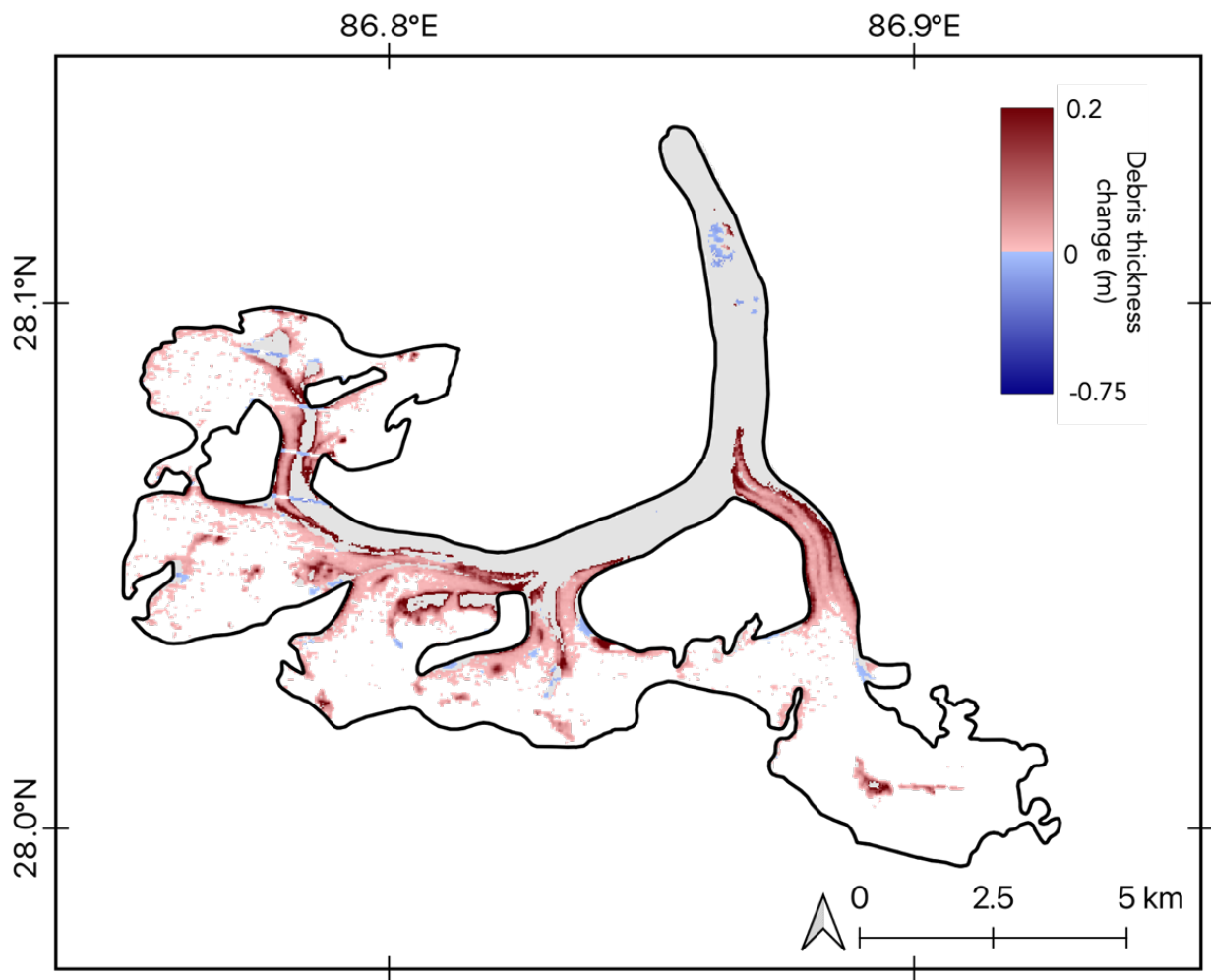


**Figure 4.5.** Significant changes in debris thickness on Rongbuk Glacier between 2000 and 2021. Grey pixels represent debris which displayed no significant change in thickness. Note that the colour bar is asymmetrical around 0 because the thinning on the lake was significantly more than the highest thickness increase.

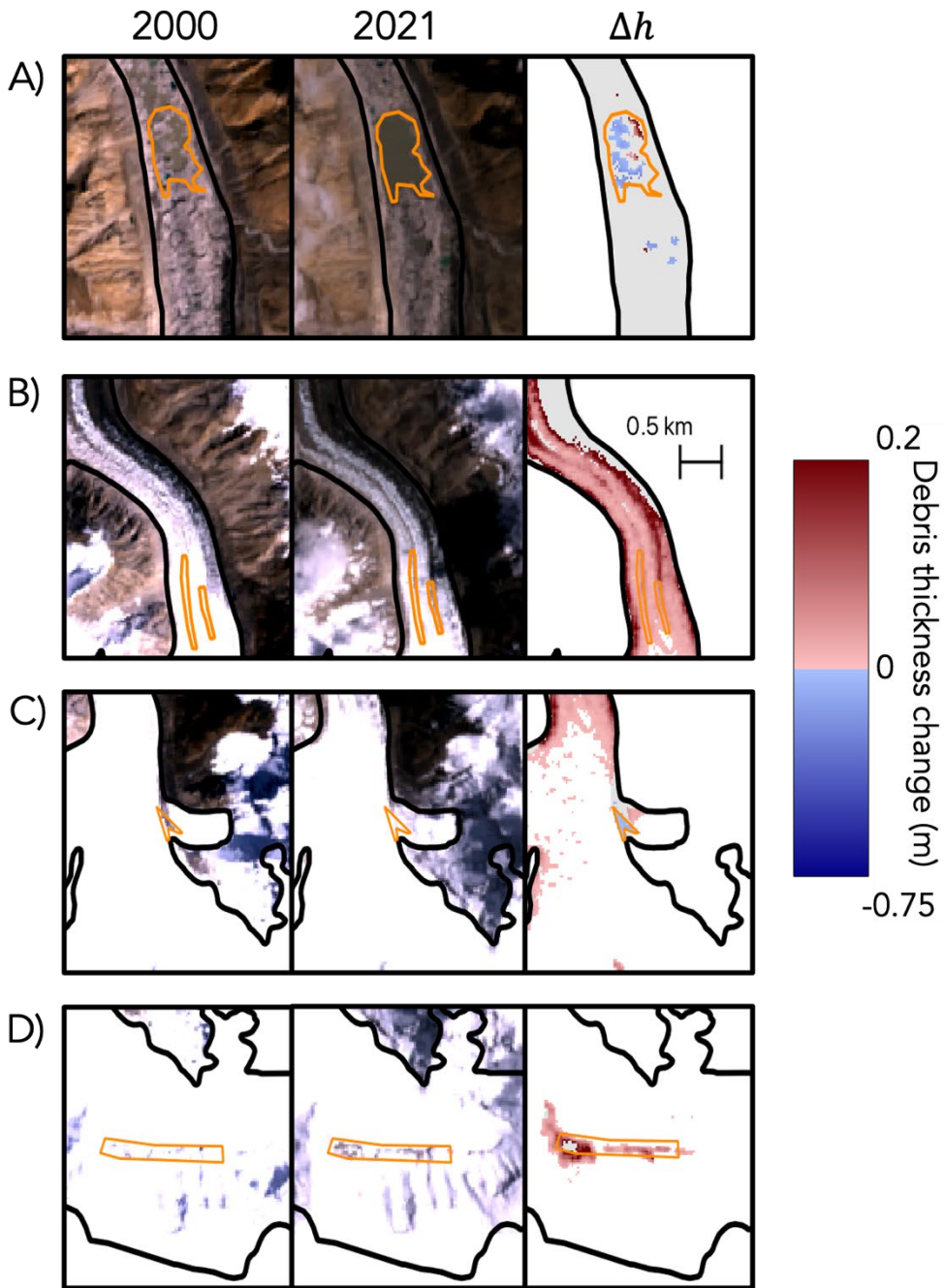


**Figure 4.6.** Visual evidence of debris thickness change between 2000 and 2021. Rows represent the two years being compared. A) the reduction in debris cover due to the expansion of the supraglacial lake. B) Expansion of medial moraine and the thickening of dirty ice and the glacier margins. C) Thinning of debris along the glacier margin. D) Thickening of debris at the base of the headwall of Mount Everest. Pixels with an insignificant change in debris cover are shown in grey. Note that the colour bar is asymmetrical around 0 because the thinning on the lake was significantly more than the highest thickness increase. Visual images are from Landsat 7 (12/09/2000 and 04/07/2021) - courtesy of the U.S. Geological Survey.

### 4.3 Estimated debris accumulation rate

Spatial patterns in DARs (Figure 4.7) reveal trends obscured by pairwise map differencing. 36.1 km<sup>2</sup> (48.9%) and 5.6 km<sup>2</sup> (7.5%) of the glacier area displayed average thickening and thinning, respectively, over the study period. Areas of thinning often align with supraglacial ponds, indicating their development. The maximum accumulation rate,  $0.027 \pm 0.012 \text{ m yr}^{-1}$ , is observed on the glacier margin on the tongue, reflecting debris input from mountainsides. The greatest thinning rate,  $-0.028 \pm 0.0087 \text{ m yr}^{-1}$ , is observed on the supraglacial lake. DARs along medial moraine and the glacier margins are typically the highest, which is likely due to an increased debris supply from mountainsides and debris-rich englacial septa.

For thinner areas, particularly in the TZ, the estimated DAR is greater than the uncertainty, typically by 2-4 times, lending confidence that debris is indeed thickening in these regions. In the TZ, the average DAR is  $1.3 \pm 0.4 \text{ mm yr}^{-1}$ . For pixels where debris thickness is already high, predominantly on the tongue and WRG, the uncertainty in the accumulation rate is generally greater than the estimated DAR. Therefore, it is uncertain whether debris is thickening or thinning. Due to the high uncertainty and limitations of the RM14 model for regions of higher debris thickness (Rounce and McKinney, 2014), this is expected.

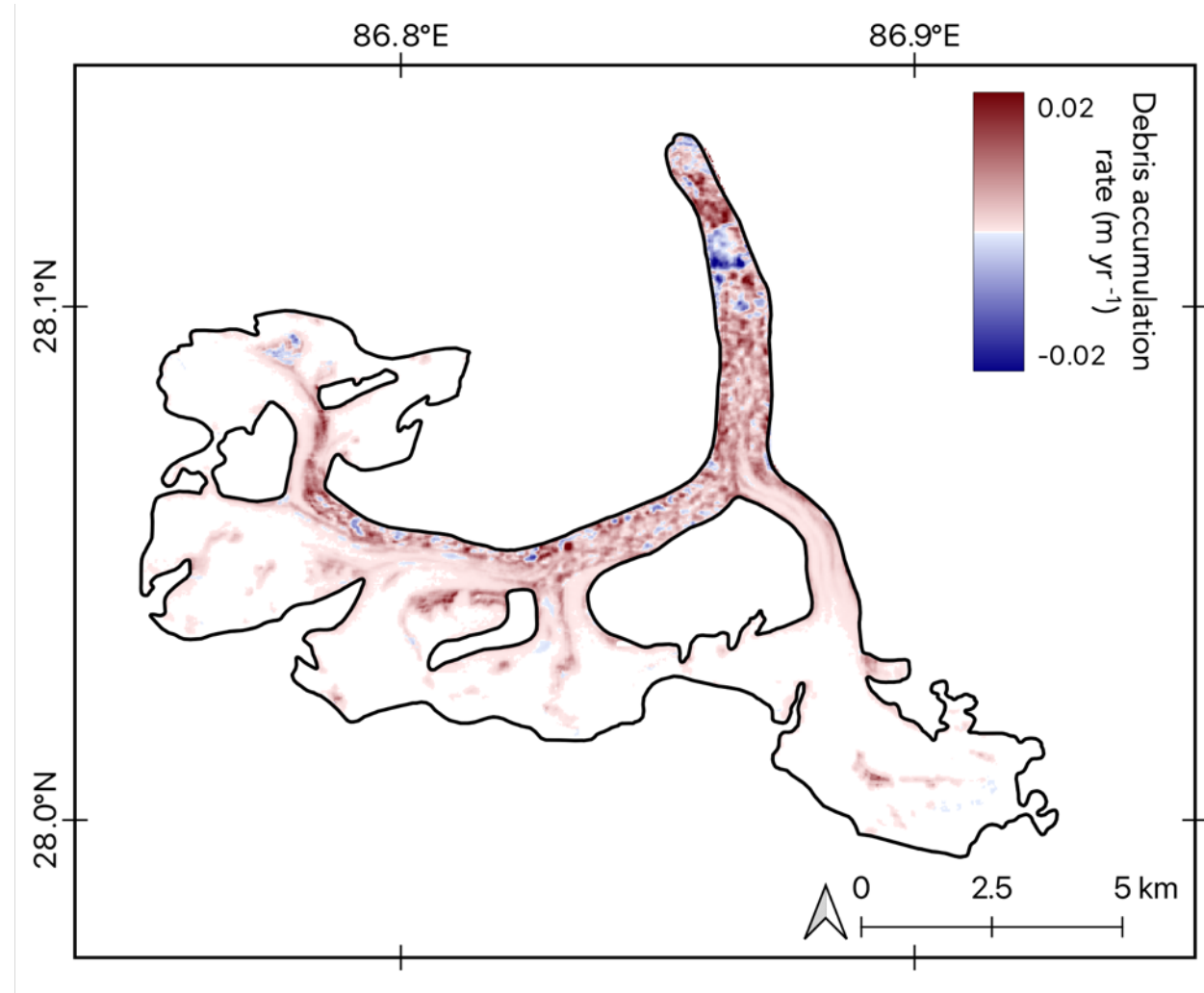


**Figure 4.7.** Estimates of the debris accumulation rate ( $\text{m yr}^{-1}$ ) across Rongbuk Glacier.

#### 4.4 Stacked distributed debris thickness maps

Stacked DDTMs (Appendix 5) reveal a more coherent pattern in debris thickening and expansion of the debris-covered area. The development of debris cover in the TZ is more discernible, whereas individual maps displayed inconsistent changes. Stacked maps clearly show the emergence of medial moraine, followed by the widening of medial and lateral moraine until their coalescence (Figure 4.8). Therefore, this supports the use of stacking multiple maps to improve the clarity of the evolution of debris cover. The final stacked DDTM, spanning 2020-2021 is hereafter referred to as the ‘present-day’ thickness (Figure 4.9).

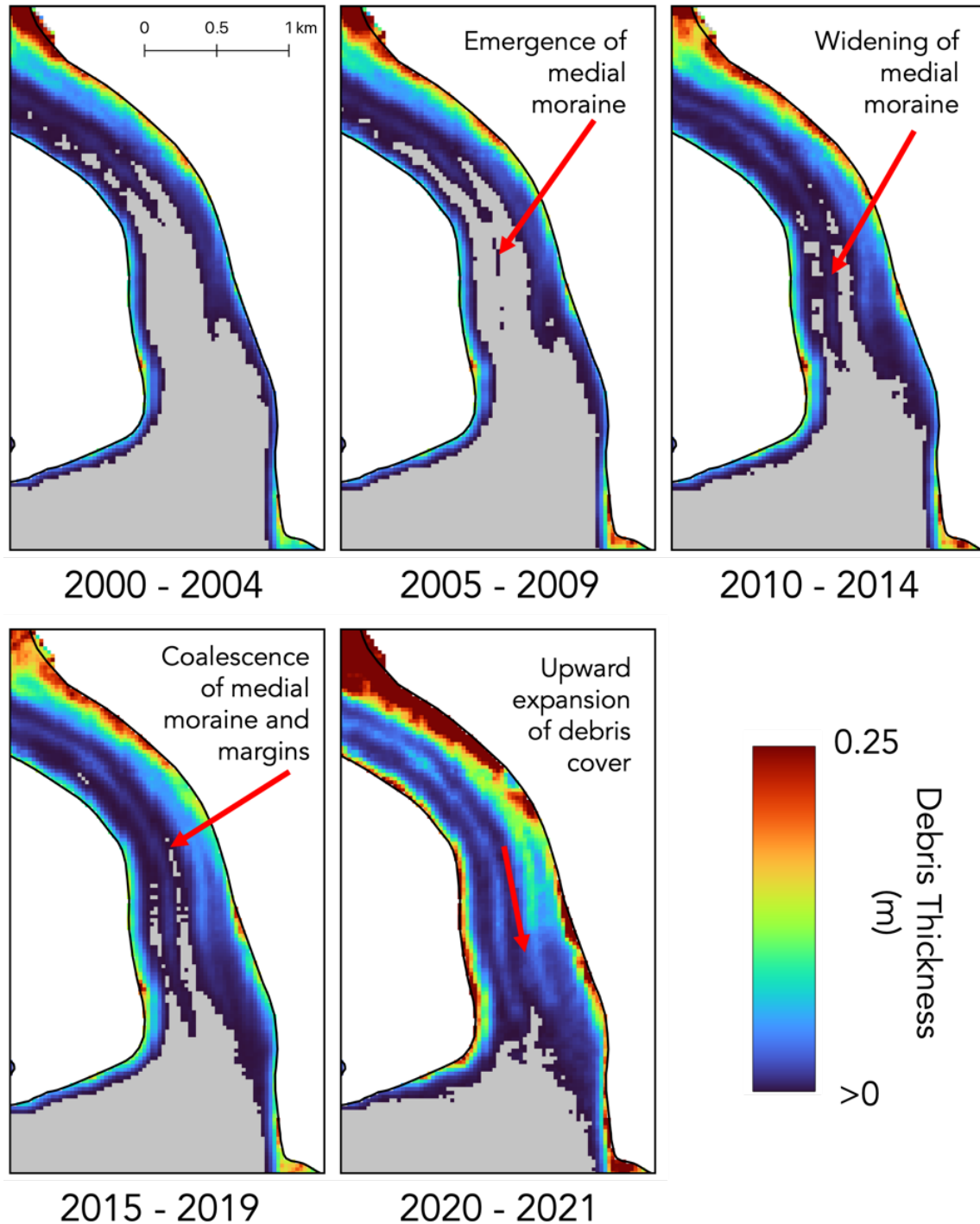


**Figure 4.8.** 5-year stacked and averaged distributed debris thickness maps for the transition zone. Grey pixels represent clean ice.

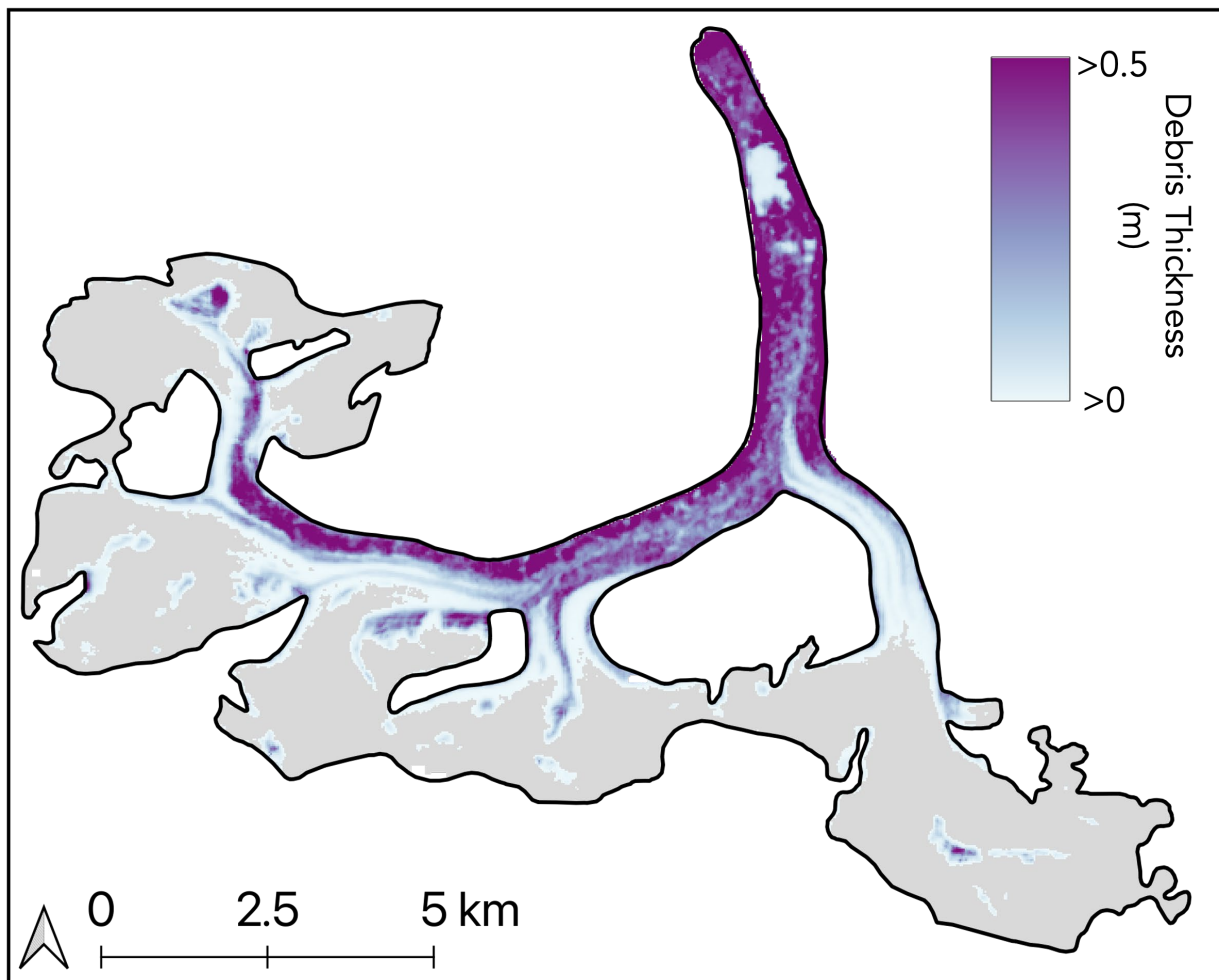


**Figure 4.9.** Present-day distributed debris thicknesses for Rongbuk Glacier.

## 5 Discussion

### 5.1 Down-glacier debris distribution

This study has derived the first estimates of debris evolution on RG, showing that debris has advanced up-glacier to higher elevations, expanding the debris-covered area. It has also showed that debris thickening has occurred. The rates of expansion in area to increased elevations,  $0.77 \text{ p.p. yr}^{-1}$  and  $5.7 \text{ m yr}^{-1}$ , respectively, are comparable with Thakuri et al.'s (2014) mean observations of  $0.20 \pm 0.06 \text{ p.p. yr}^{-1}$  and  $3.7 \pm 0.5 \text{ m yr}^{-1}$ , respectively, for HMA. The use of a single glacier outline may have resulted in overestimates of the increase in the debris-covered fraction because newly exposed valley sides due to terminus retreat or surface lowering would still be classified as debris (Scherler et al., 2018). Improved outlining methods would provide better estimates of the debris-covered fraction evolution, though this is difficult owing to RG's thick debris along its margins and terminus, which has a similar reflectance in satellite imagery to bare valley sides (Paul et al., 2004).

The supraglacial debris distribution on RG agrees with both field observations and numerical modelling of debris thickness, displaying a down-glacier increase in thickness and increased accumulation along glacier margins and medial moraine zones (Kirkbride and Deline, 2013; Anderson and Anderson, 2018; Rounce et al., 2021). Two regimes of down-glacier debris thickening are observed on the MRG and WMRG. The first is the increase in debris thickness down-glacier within the TZ up to the confluence of the MRG and WRG, indicative of a monotonic slowdown in the glacier velocity toward the confluence of the two glaciers (Anderson and Anderson, 2018). This pattern agrees with surface velocity estimates of RG from global datasets (Figure 1.2) (Gardner et al., 2022). Second is the increase in debris thickness down-glacier on the tongue. At face value, this would also indicate a monotonic decline in the glacier's velocity here. However, the tongue is stagnant. Therefore, rather than showing the glacier's current velocity regime, the tongue's debris distribution is indicative of a past regime which has since ceased. Consequently, an important distinction needs to be made: monotonic decreases in glacier velocity toward the terminus will result in an increase in debris thickness down-glacier. However, observations of debris thickness increasing down-glacier do not necessarily imply a current monotonically decreasing velocity regime. They only imply that this regime was present previously, lasting for a sufficient time for the debris distribution to occur. Therefore, DDTMs can aid the interpretation of former glacial systems (Hambrey and Glasser, 2012). A similar regime is observed and predicted for Khumbu Glacier, where its tongue, due to increased surface lowering at its upper end, is predicted to disconnect entirely from the active part of the glacier,

which is predicted to form a new debris-covered tongue (Rowan et al., 2015). It is therefore likely that RG may face a similar future.

## 5.2 Study comparison

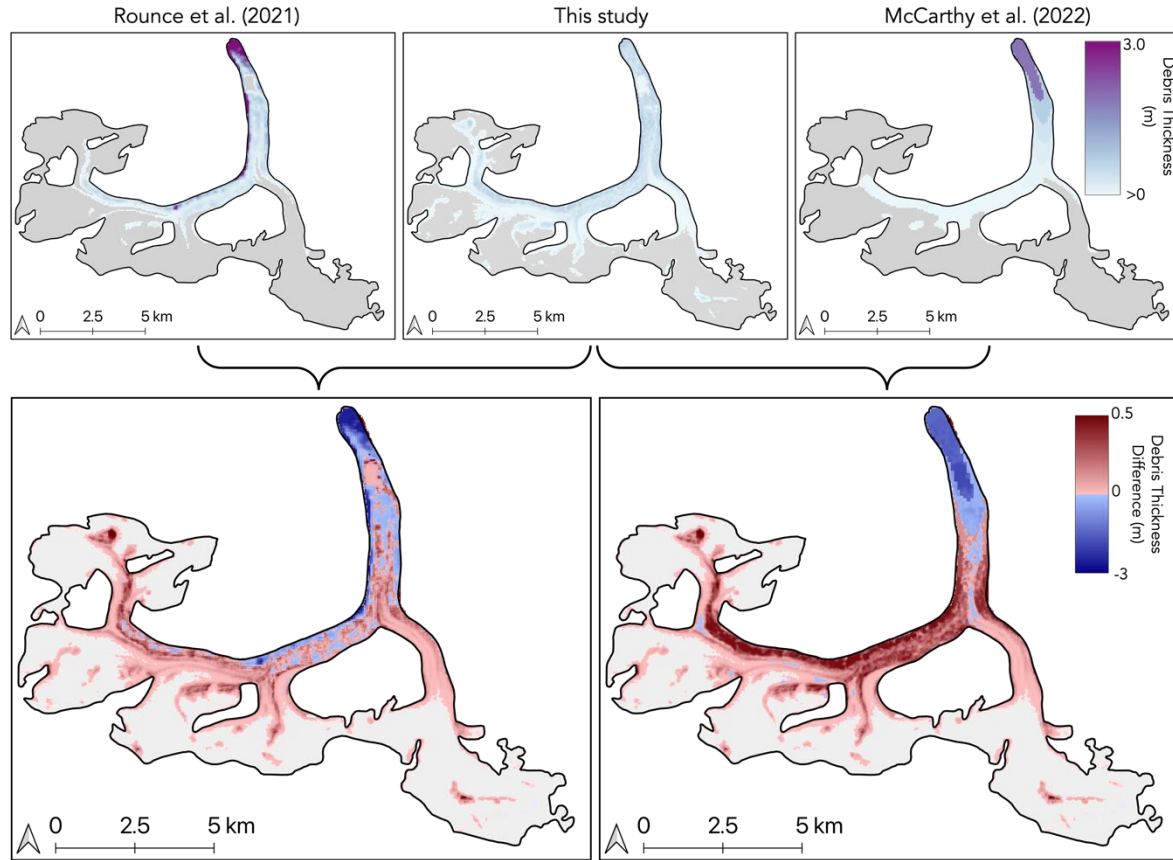


**Figure 5.1.** Top: distributed debris thickness estimates for Rongbuk Glacier from this study, Rounce et al. (2021), and McCarthy et al. (2022). Bottom: Comparison maps between this study and Rounce et al.’s (2021) and McCarthy et al.’s (2022) estimates for distributed debris thicknesses over Rongbuk Glacier. All model estimates were resampled to match the pixel alignment of this study’s model outputs before differencing.

This study has produced a third physics-derived DDTM of the present-day RG. Comparisons with R21 and M22 (Figure 5.1) show that this study underestimates debris thickness towards RG’s tongue. This is expected owing to the RM14 model’s inability to reliably quantify debris  $>0.5$  m thick. This study has estimated debris cover on the tongue and much of the WRG as 0.5–0.8 m thick, though the true range is likely to extend well beyond 0.8 m because R21 and M22 both estimate debris thicknesses of up to 3 m on the tongue and margins. Meanwhile, this study

overestimates debris thicknesses further from the tongue, especially in the TZ. It also detects a much larger debris-covered area due to its detection of medial moraine extending further up-glacier and adjacent dirty ice. Indeed, this study finds that RG is 42.9% debris covered, compared with 20.4% and 21.0% from the R21 and M22 models, respectively. Without *in situ* measurements of debris thickness, it is not possible to verify which model's results are more accurate. However, this model's detection of dirty ice has implications for how dirty ice is represented in debris thickness models (Section 5.4).

### 5.3 The use of temporal trends in the debris evolution workflow

Both temporal approaches (stacked averages and DARs) clearly show that debris emergence is greatest along medial moraines and on the glacier margins and that debris cover is expanding up-glacier. However, both methods remain limited by their derivation from the RM14 model, which (i) is limited to debris  $<0.5$  m thick and (ii) still struggles with individual variability, which could skew trends. Improving upon these limitations would provide better estimates, discussed in Section 5.4.

The mean DAR in the TZ is  $1.3 \pm 0.4$  mm yr $^{-1}$ , which translates to a 10 cm increase in debris thickness by the EOC. This is an overestimate compared to Compagno et al.'s (2022) estimate of 2 cm for HMA, but within an order of magnitude. This overestimate highlights a limitation of performing linear regression to estimate the mean DAR over the study period because, as debris thickens, the DAR due to meltout will decrease owing to the non-linear nature of the Østrem Curve (Section 1.2.1). Therefore, while regression provides insight into recent trends, longer-term projections should consider dynamic feedbacks between melt suppression and debris evolution.

Another key limitation is this study's omission of correcting for glacier flow. Consequently, debris-covered pixels were treated in a fixed reference frame. Thus, equivalent pixels within each DDTM will not showcase the same on-glacier debris, limiting this study's direct comparison of pixels, whether in differencing, stacking, or regression. Parts of the MRG are moving upwards of 30–45 m yr $^{-1}$  (Gardner et al., 2022). Given Landsat 7's resolution of 30 x 30 m, a given parcel of debris may be moved to a different pixel each year.

Nonetheless, meaningful conclusions can still be drawn. In a steady-state system, each pixel's *observed* DAR would approach zero because the accumulation and evacuation rates of debris are in balance (Anderson and Anderson, 2016, 2018). Therefore, detecting a DAR, even in pixels where the glacier is moving, demonstrates that the system is not in a steady state. This suggests either an increase in debris input, a reduction in evacuation efficiency, or both. Whilst a non-steady-state was indirectly assumed given this study's aims of monitoring debris cover's upward

expansion, spatial patterns in the DARs can offer insights into the mechanisms driving increased accumulation.

Increases in debris accumulation can be attributed to enhanced ice melt or an increase in englacial debris composition, which is associated with an increased debris supply rate up-glacier from mountainsides (Kirkbride and Deline, 2013). Apportioning the contribution of each is difficult. Surface lowering on RG has generally accelerated in recent decades (Ye et al., 2022), likely contributing to increased meltout. However, debris compositions within glacier ice are generally understudied, with some exceptions (e.g., Miles et al., 2021), meaning the estimated debris contribution from increased meltout is unknown. Nevertheless, this study has developed a spatial map of DARs where assumptions can be made about the contribution of each. For example, debris has accumulated at the base of the steep headwall of Mount Everest at a mean rate of  $5.5 \pm 1.2 \text{ mm yr}^{-1}$  (Figure 5.2). At an elevation of 6,200 m, 300-500 m above the estimated present-day ELA for Khumbu Glacier (Bolch et al., 2011; Rowan et al., 2015), debris meltout is implausible at this elevation, and localised increases in debris thickness must be attributed to an increase in debris deposition from mountainsides. Although the magnitude of accumulation may be limited due to the RM14 model's limitations in the accumulation zone (Section 5.4), it provides compelling evidence that debris delivery from mountainsides is increasing, possibly due to reduced snow cover on mountain faces resulting in more rockfalls (Deline, 2009), likely contributing to an enhanced englacial debris composition.

There is, however, a lag time between increased debris supply in the upper glacier and its emergence in the ablation zone (Kirkbride and Deline, 2013). Given the headwall is  $>3 \text{ km}$  up-glacier from the zone of initial debris emergence, and a glacier flow velocity of  $40 \text{ m yr}^{-1}$  (Gardner et al., 2022), it would take  $\sim 75$  years for an increased debris supply from the headwall to contribute to increased debris emergence, which is beyond the observational length of this study. Nonetheless, it may serve as an indicator of the future of debris evolution on RG if enhanced debris supply persists. Debris emergence rates will be accelerated independently of, and in addition to, those driven by rising temperatures (Kirkbride and Deline, 2013). The compound effect is the accelerated development of continuous debris cover, shortening the length of the TZ where patchy debris cover enhances melt, thereby decreasing the upper glacier's vulnerability to climate change. This has important implications for improving current predictive models of debris evolution, which assume a homogenous englacial debris composition (Compagno et al., 2022).

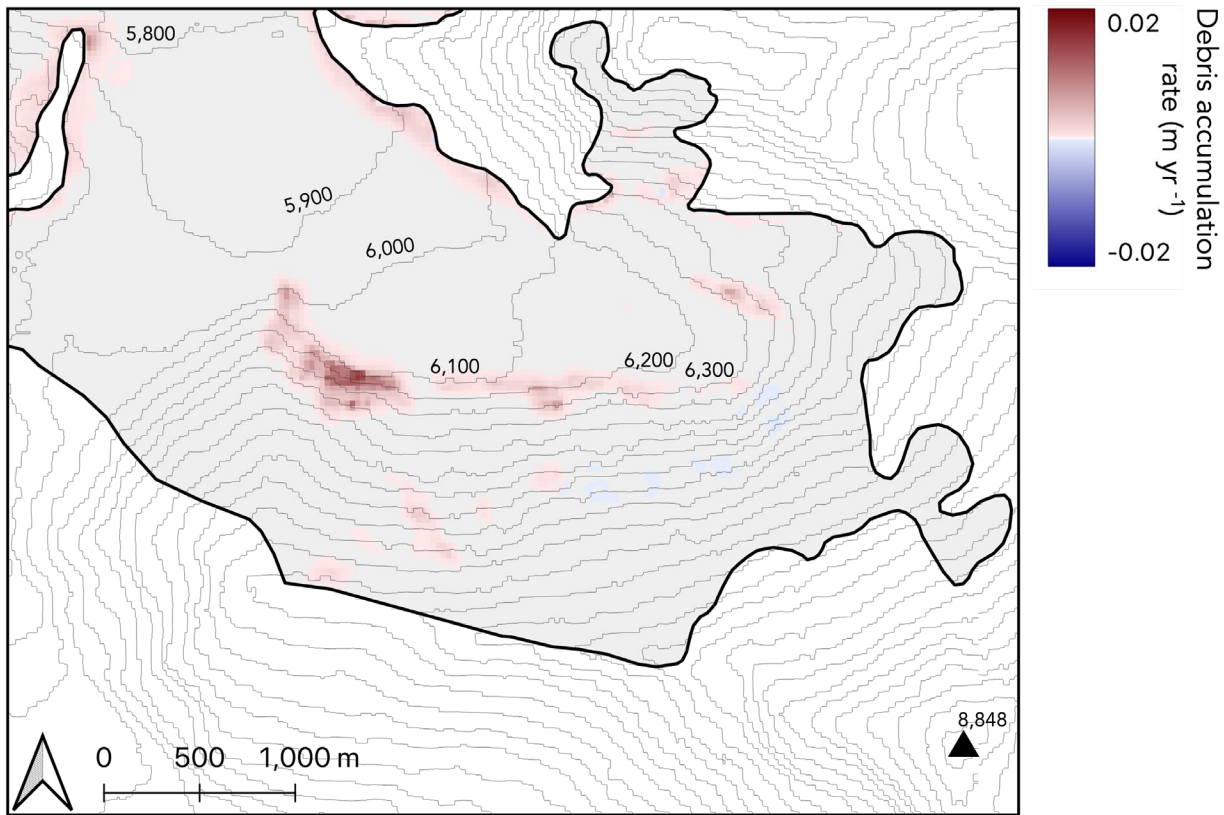


**Figure 5.2.** Debris accumulation rates ( $\text{m yr}^{-1}$ ) at the base of the steep headwall of Mount Everest. 100 m contour lines are shown to emphasise the relief. Mount Everest's peak, at 8,848 m is shown in the bottom right. Debris can be clearly seen accumulating at the base of the headwall. Thinning higher up is indicative of the redistribution of debris on the headwall.

## 5.4 Model-specific limitations and areas for future research

This section discusses key limitations and assumptions of the RM14 model and their implications for estimating debris thickness in the TZ, where debris cover is sparse and patchy. While this study implemented methods to mitigate variability between DDTMs, certain scenes (e.g., 28/07/2018 and 13/06/2019, Section 4.1) clearly underestimate both thickness and extent, which affects derived trends.

Beyond commonly acknowledged and discussed simplifications such as spatially homogeneous meteorological and debris properties (Rounce and McKinney, 2014), the RM14 model makes two key assumptions which are deemed as particularly relevant for this study and where discussion is minimal. First, it assumes that any pixel with a temperature above 273.15 K must be debris-covered. Second, it assumes that the debris-ice interface is at 273.15 K. The RM14 model then estimates debris

thickness based on the temperature difference and a modelled temperature gradient (Rounce and McKinney, 2014).

Firstly, this results in water-covered pixels being registered as debris-covered because they are  $>273.15\text{ K}$ . This differs from the mixed pixel effect discussed by Rounce et al (2018), which refers to ice cliffs and supraglacial ponds small enough to fit into a single pixel, affecting debris thickness estimates. Rather, this refers to pixels which are entirely water-covered, of which there are many on RG. Whilst this study has asserted that RG's tongue is almost entirely debris-covered, in reality, it is almost entirely debris-covered *or* water-covered (with a fraction of ice cliffs). This has implications for assessing the melt regime on RG's tongue because supraglacial ponds present highly localised regions of melt, which could even offset the reduced ablation beneath thick debris on the tongue, which is regarded as the 'debris-cover anomaly' (Salerno et al., 2017). Rounce et al. (2018) solve this issue by delineating supraglacial ponds and ice cliffs using high-resolution imagery and removing them from debris thickness estimates. Without delineating supraglacial ponds on RG's tongue, whose shapes evolve in every DDTM, the tongue's debris-covered area is likely to be overestimated.

The implications of these assumptions in the TZ are more important still. In many cases, debris was evident in visual imagery, yet wasn't detected. These pixels exhibited surface temperatures  $<273.15\text{ K}$ , thus violating the assumption that debris must raise pixel temperatures above the melting point. Therefore, whilst the assumption that pixels  $>273.15\text{ K}$  must be debris covered is still valid (ice cannot be  $>273.15\text{ K}$ ), it fails to recognise that debris could be  $<273.15\text{ K}$ . There are several plausible explanations for this discrepancy (Figure 5.3): (i) The entire pixel is debris-covered, and the debris is  $<273.15\text{ K}$ . (ii) The pixel is partially debris-covered, the debris itself is  $>273.15\text{ K}$ , but the clean ice cools the observed temperature to  $<273.15\text{ K}$ . (iii) The pixel is partially debris-covered, but both the debris and clean ice are  $<273.15\text{ K}$ . Or a combination of (ii) and (iii).

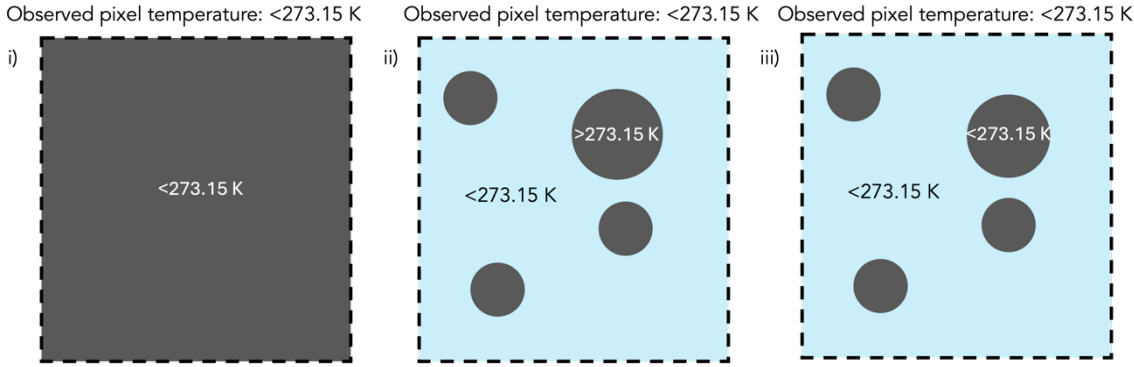


**Figure 5.3.** Explanations for why debris is observed to be below 273.15 K in certain pixels. Each option presents a single pixel and speculation for what its sub-pixel level composition may be.

The TZ consists of patchy debris cover (Fyffe et al., 2020), supporting scenarios (ii) and (iii). Therefore, the mixed pixel effect plays a large role and if it is sufficiently strong to cool the pixel's observed temperature to  $<273.15\text{ K}$ , even if debris is  $>273.15\text{ K}$ , then there is no debris detection. High-resolution studies of debris surface temperatures using UAVs show significant temperature variability (e.g., Kraaijenbrink et al., 2018). However, they do not cover the upper ablation area. Further studies with UAVs over the TZ would provide more insight into the temperature range for discontinuous debris. Given that the model also, on occasion, fails to quantify the more clearly defined medial moraine, which is mostly continuously covered within a pixel, it indicates that the debris surface temperature can indeed be  $<273.15\text{ K}$ . Therefore, dynamic energy-balance modelling (e.g., Reid and Brock, 2010), which considers perhaps the influence of a cold night before Landsat acquisition, may be required to better represent the energy balance at the time of Landsat acquisition than what can currently be offered with instantaneous energy balance modelling (Schauwecker et al., 2015).

Moreover, *if* the debris surface temperature can be  $<273.15\text{ K}$ , then it follows that the debris-ice interface may also be  $<273.15\text{ K}$ , thereby violating the RM14 model's second key assumption. On the one hand, the model is operating in the ablation season and therefore ice is assumed to have warmed sufficiently to the freezing point. However, the TZ is at a higher elevation and may not consistently be in the ablation area – the ELA varies year to year (Sakai and Fujita, 2017). This assumption has further implications for debris quantified within the accumulation zone. Although this study quantified debris in the accumulation zone, indicating the surface temperature was above freezing, the debris-ice interface could remain below freezing owing to sustained cold temperatures at high elevations. Thus, the debris thickness is likely to be underestimated. Under current modelling frameworks (Section 1.2.4.2), no model can quantify debris thickness in the accumulation zone. STIMs fail for the reasons stated above. DAIMs fail, even with correcting for glacier flow, because

debris will have no influence on net melt – no net melt is occurring. Whilst unimportant for assessing the current melt rate of the glacier, this has implications for assessing what future melt rates may be from this debris being advected and later emerging down-glacier. This represents a key limitation in remote sensing-based debris thickness modelling and highlights an important area for future research.

In essence, the RM14 model produces a binary output – debris is present (and has a quantifiable thickness) or not. Whilst this approach is beneficial and applicable globally using coarse-resolution satellite imagery, it is poorly suited for the TZ, where pixels contain a fractional debris cover (Fyffe et al., 2020). Although this study detects debris cover across much of the TZ, comparison with photographs of RG (Figure 5.4) reveals that debris is sparse and confined to topographic lows between seracs due to gravitational redistribution. This underscores the need to move beyond binary classification in debris detection. A method for estimating fractional debris cover would greatly improve debris thickness estimates in the TZ. Ideally, high-resolution thermal data would be used, which would largely omit any requirement for quantifying fractional debris cover. However, this is impractical for regional or global applications.

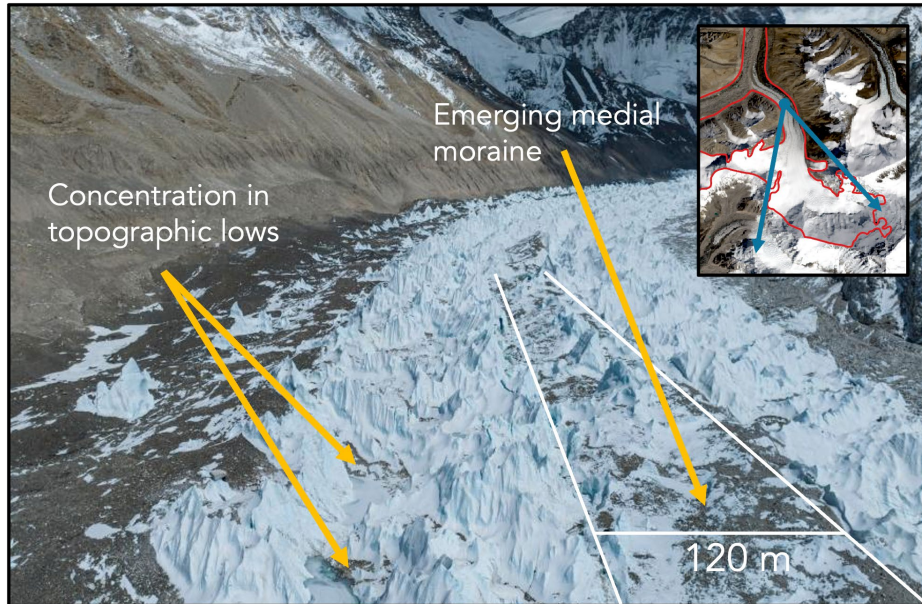


**Figure 5.4.** Image showing the reality of debris cover on Rongbuk Glacier's transition zone. Debris is discontinuous, which is not implied from the model outputs. Image from China Daily (2023). The location of the photo in relation to Rongbuk Glacier is shown in the top right.

## 6 Conclusions

This study aimed to quantify changes to debris thickness and extent on RG using Landsat 7 thermal imagery and energy balance modelling. This is important because the evolution of debris cover, especially in the TZ, remains poorly understood, and ice melt is highly sensitive to discontinuous debris cover.

This study generated a time series of DDTMs between 2000 and 2021. Using map differencing and uncertainty thresholds, over the study period, RG's debris-covered area expanded by 14.8 p.p., and its mean debris thickness increased from  $0.14 \pm 0.05$  m to  $0.21 \pm 0.06$  m. Most changes to debris cover were in the TZ, which reflects the RM14 model's limited sensitivity to thicker debris cover. Combined, these correspond to a net volume gain of  $434,000 \pm 20,000$  m<sup>3</sup>. These results, however, are limited in their derivation from the differencing of individual debris thickness maps, which show significant variability. Therefore, this study encourages the use of temporal trends over the study period.

This study introduced two methods of doing so: stacking maps into 5-year averages and pixel-wise linear regression, and hence, defined the 'debris accumulation rate'. 5-year averages clearly show the evolution of debris emergence in concentrated medial moraine and the expansion of medial moraine until coalescence to form continuous debris cover. Pixel-wise linear regression demonstrates debris thickening ( $1.3 \pm 0.4$  mm yr<sup>-1</sup> in the TZ) and provides compelling evidence that the debris supply from mountainsides is increasing, which could be a cause of enhanced debris emergence down-glacier. Including increased debris input into current debris evolution models would allow for better projections of the evolution of debris cover.

Physics-based models struggle to consistently quantify debris cover in the TZ. Dynamic energy balance modelling would allow for a better understanding of the energy balance at the time of Landsat acquisition. However, this is computationally expensive. Furthermore, methods for estimating the fractional debris cover within low-resolution satellite-obtained pixels need to be developed so that the sparsely covered TZ can be better represented in models of debris cover and its evolution, thereby permitting better projections of debris evolution and its resultant impacts on glacier dynamics in a changing climate.

## 7 References

- Abrams, M. *et al.* (2010) ‘The aster global dem’, *Photogrammetric Engineering and Remote Sensing*, 76(4), pp. 344–348.
- Adhikary, S. *et al.* (1997) ‘Effect of surface dust on snow melt’, *Bulletin of glacier research*, (15), pp. 85–92.
- Adhikary, S. *et al.* (2000) ‘Dust influence on the melting process of glacier ice: experimental results from Lirung Glacier, Nepal Himalayas, chap’, *Debris-Covered Glaciers*, pp. 43–52.
- Anderson, L.S. and Anderson, R.S. (2016) ‘Modeling debris-covered glaciers: response to steady debris deposition’, *The Cryosphere*, 10(3), pp. 1105–1124. Available at: <https://doi.org/10.5194/tc-10-1105-2016>.
- Anderson, L.S. and Anderson, R.S. (2018) ‘Debris thickness patterns on debris-covered glaciers’, *Geomorphology*, 311, pp. 1–12. Available at: <https://doi.org/10.1016/j.geomorph.2018.03.014>.
- Anderson, R.S. (2000) ‘A model of ablation-dominated medial moraines and the generation of debris-mantled glacier snouts’, *Journal of Glaciology*, 46(154), pp. 459–469. Available at: <https://doi.org/10.3189/172756500781833025>.
- Aubry-Wake, C. *et al.* (2023) ‘Using ground-based thermal imagery to estimate debris thickness over glacial ice: fieldwork considerations to improve the effectiveness’, *Journal of Glaciology*, 69(274), pp. 353–369. Available at: <https://doi.org/10.1017/jog.2022.67>.
- Bartlett, O.T. *et al.* (2021) ‘Morphology and evolution of supraglacial hummocks on debris-covered Himalayan glaciers’, *Earth Surface Processes and Landforms*, 46(3), pp. 525–539. Available at: <https://doi.org/10.1002/esp.5043>.
- Benn, D. and Owen, L. (2002) ‘Himalayan glacial sedimentary environments: A framework for reconstructing and dating the former extent of glaciers in high mountains’, *Quaternary International*, 97–98, pp. 3–25. Available at: [https://doi.org/10.1016/S1040-6182\(02\)00048-4](https://doi.org/10.1016/S1040-6182(02)00048-4).
- Benn, D.I. *et al.* (2012) ‘Response of debris-covered glaciers in the Mount Everest region to recent warming, and implications for outburst flood hazards’, *Earth-Science Reviews*, 114(1), pp. 156–174. Available at: <https://doi.org/10.1016/j.earscirev.2012.03.008>.

- Benn, D.I. *et al.* (2017) ‘Structure and evolution of the drainage system of a Himalayan debris-covered glacier, and its relationship with patterns of mass loss’, *The Cryosphere*, 11(5), pp. 2247–2264. Available at: <https://doi.org/10.5194/tc-11-2247-2017>.
- Biemans, H. *et al.* (2019) ‘Importance of snow and glacier meltwater for agriculture on the Indo-Gangetic Plain’, *Nature Sustainability*, 2(7), pp. 594–601. Available at: <https://doi.org/10.1038/s41893-019-0305-3>.
- Bolch, T. *et al.* (2011) ‘Multi-decadal mass loss of glaciers in the Everest area (Nepal Himalaya) derived from stereo imagery’, *The Cryosphere*, 5(2), pp. 349–358. Available at: <https://doi.org/10.5194/tc-5-349-2011>.
- Boulton, G. (1978) ‘Boulder shapes and grain-size distributions of debris as indicators of transport paths through a glacier and till genesis’, *Sedimentology*, 25, pp. 773–799.
- Boxall, K. *et al.* (2021) ‘Quantifying Patterns of Supraglacial Debris Thickness and Their Glaciological Controls in High Mountain Asia’, *Frontiers in Earth Science*, 9. Available at: <https://doi.org/10.3389/feart.2021.657440>.
- Brock, B. *et al.* (2007) ‘The surface energy balance of an active ice-covered volcano: Villarrica Volcano, southern Chile’, *Annals of Glaciology*, 45, pp. 104–114. Available at: <https://doi.org/10.3189/172756407782282372>.
- Brock, B.W. *et al.* (2010) ‘Meteorology and surface energy fluxes in the 2005–2007 ablation seasons at the Miage debris-covered glacier, Mont Blanc Massif, Italian Alps’, *Journal of Geophysical Research: Atmospheres*, 115(D9). Available at: <https://doi.org/10.1029/2009JD013224>.
- Brun, F. *et al.* (2018) ‘Ice cliff contribution to the tongue-wide ablation of Changri Nup Glacier, Nepal, central Himalaya’, *The Cryosphere*, 12(11), pp. 3439–3457. Available at: <https://doi.org/10.5194/tc-12-3439-2018>.
- C3S (2017) ‘ERA5: Fifth Generation of ECMWF Atmospheric Reanalyses of the Global Climate’. Copernicus Climate Change Service Climate Data Store (CDS). Available at: <https://www.ecmwf.int/en/forecasts/dataset/ecmwf-reanalysis-v5>.
- China Daily (2023) *Rongbuk flows quietly at Mount Qomolangma's foot*, chinadailyhk. Available at: <https://www.chinadailyhk.com/hk/article/331577#Rongbuk-flows-quietly-at-Mount-Qomolangma's-foot-2023-05-18> (Accessed: 18 December 2024).
- Coll, Cé. *et al.* (2010) ‘Validation of Landsat-7/ETM+ Thermal-Band Calibration and Atmospheric Correction With Ground-Based Measurements’, *IEEE Transactions on Geoscience and Remote Sensing*, 48(1), pp. 547–555. Available at: <https://doi.org/10.1109/TGRS.2009.2024934>.

- Compagno, L. *et al.* (2022) ‘Modelling supraglacial debris-cover evolution from the single-glacier to the regional scale: an application to High Mountain Asia’, *The Cryosphere*, 16, pp. 1697–1718. Available at: <https://doi.org/10.5194/tc-16-1697-2022>.
- Deline, P. (2009) ‘Interactions between rock avalanches and glaciers in the Mont Blanc massif during the late Holocene’, *Quaternary Science Reviews*, 28(11), pp. 1070–1083. Available at: <https://doi.org/10.1016/j.quascirev.2008.09.025>.
- Edwards, T.L. *et al.* (2021) ‘Projected land ice contributions to twenty-first-century sea level rise’, *Nature*, 593(7857), pp. 74–82. Available at: <https://doi.org/10.1038/s41586-021-03302-y>.
- Evatt, G.W. *et al.* (2015) ‘Glacial melt under a porous debris layer’, *Journal of Glaciology*, 61(229), pp. 825–836. Available at: <https://doi.org/10.3189/2015JoG14J235>.
- Farinotti, D. *et al.* (2019) ‘Large hydropower and water-storage potential in future glacier-free basins’, *Nature*, 575(7782), pp. 341–344. Available at: <https://doi.org/10.1038/s41586-019-1740-z>.
- Fontrodona-Bach, A. *et al.* (2025) ‘DebDab: A database of supraglacial debris thickness and physical properties’, *Earth System Science Data Discussions*, pp. 1–34. Available at: <https://doi.org/10.5194/essd-2024-559>.
- Foster, L.A. *et al.* (2012) ‘A physically based method for estimating supraglacial debris thickness from thermal band remote-sensing data’, *Journal of Glaciology*, 58(210), pp. 677–691. Available at: <https://doi.org/10.3189/2012JoG11J194>.
- Fujisada, H. *et al.* (2005) ‘ASTER DEM performance’, *IEEE Transactions on Geoscience and Remote Sensing*, 43(12), pp. 2707–2714. Available at: <https://doi.org/10.1109/TGRS.2005.847924>.
- Fyffe, C.L. *et al.* (2014) ‘A distributed energy-balance melt model of an alpine debris-covered glacier’, *Journal of Glaciology*, 60(221), pp. 587–602. Available at: <https://doi.org/10.3189/2014JoG13J148>.
- Fyffe, C.L. *et al.* (2019) ‘Do debris-covered glaciers demonstrate distinctive hydrological behaviour compared to clean glaciers?’, *Journal of Hydrology*, 570, pp. 584–597. Available at: <https://doi.org/10.1016/j.jhydrol.2018.12.069>.
- Fyffe, C.L. *et al.* (2020) ‘Processes at the margins of supraglacial debris cover: Quantifying dirty ice ablation and debris redistribution’, *Earth Surface Processes and Landforms*, 45(10), pp. 2272–2290. Available at: <https://doi.org/10.1002/esp.4879>.

- Gardner, A. *et al.* (2022) ‘MEaSUREs ITS\_LIVE regional glacier and ice sheet surface velocities, version 1’, (*No Title*) [Preprint].
- Gibson, M.J. *et al.* (2017) ‘Temporal variations in supraglacial debris distribution on Baltoro Glacier, Karakoram between 2001 and 2012’, *Geomorphology*, 295, pp. 572–585. Available at: <https://doi.org/10.1016/j.geomorph.2017.08.012>.
- Gillman, P. (1993) *Everest - The Best Writing and Pictures from Seventy Years of Human Endeavour*. Little, Brown and Company.
- Goodsell, B. *et al.* (2005) ‘Debris transport in a temperate valley glacier: Haut Glacier d’Arolla, Valais, Switzerland’, *Journal of Glaciology*, 51(172), pp. 139–146. Available at: <https://doi.org/10.3189/172756505781829647>.
- Gorelick, N. *et al.* (2017) ‘Google Earth Engine: Planetary-scale geospatial analysis for everyone’, *Remote Sensing of Environment*, 202, pp. 18–27. Available at: <https://doi.org/10.1016/j.rse.2017.06.031>.
- Grace, J. (2019) ‘How to Adjust for Spatial Autocorrelation’. (Open-File Report). Available at: [https://d9-wret.s3.us-west-2.amazonaws.com/assets/palladium/production/s3fs-public/media/files/61\\_SEM\\_11\\_4\\_v3-%20How%20to%20Adjust%20for%20Spatial%20Autocorrelation.pdf](https://d9-wret.s3.us-west-2.amazonaws.com/assets/palladium/production/s3fs-public/media/files/61_SEM_11_4_v3-%20How%20to%20Adjust%20for%20Spatial%20Autocorrelation.pdf) (Accessed: 4 February 2025).
- Griffith, D.A. (2005) ‘Effective Geographic Sample Size in the Presence of Spatial Autocorrelation’, *Annals of the Association of American Geographers*, 95(4), pp. 740–760. Available at: <https://doi.org/10.1111/j.1467-8306.2005.00484.x>.
- Hambrey, M.J. *et al.* (2008) ‘Sedimentological, geomorphological and dynamic context of debris-mantled glaciers, Mount Everest (Sagarmatha) region, Nepal’, *Quaternary Science Reviews*, 27(25), pp. 2361–2389. Available at: <https://doi.org/10.1016/j.quascirev.2008.08.010>.
- Hambrey, M.J. and Glasser, N.F. (2012) ‘Discriminating glacier thermal and dynamic regimes in the sedimentary record’, *Sedimentary Geology*, 251–252, pp. 1–33. Available at: <https://doi.org/10.1016/j.sedgeo.2012.01.008>.
- Herreid, S. and Pellicciotti, F. (2020) ‘The state of rock debris covering Earth’s glaciers’, *Nature Geoscience*, 13. Available at: <https://doi.org/10.1038/s41561-020-0615-0>.
- Hersbach, H. *et al.* (2018) ‘ERA5 hourly data on single levels from 1979 to present’, *Copernicus climate change service (c3s) climate data store (cds)*, 10(10.24381).

Heuvelink, G.B.M. (1998) *Error Propagation in Environmental Modelling with GIS*. London: CRC Press. Available at: <https://doi.org/10.4324/9780203016114>.

Hinkel, K.M. (1997) ‘Estimating seasonal values of thermal diffusivity in thawed and frozen soils using temperature time series’, *Cold Regions Science and Technology*, 26(1), pp. 1–15. Available at: [https://doi.org/10.1016/S0165-232X\(97\)00004-9](https://doi.org/10.1016/S0165-232X(97)00004-9).

Hock, R. *et al.* (2019) ‘GlacierMIP – A model intercomparison of global-scale glacier mass-balance models and projections’, *Journal of Glaciology*, 65(251), pp. 453–467. Available at: <https://doi.org/10.1017/jog.2019.22>.

Hock, R. and Noetzli, C. (1997) ‘Areal melt and discharge modelling of Storglaciären, Sweden’, *Annals of Glaciology*, 24, pp. 211–216. Available at: <https://doi.org/10.3189/S0260305500012192>.

Huss, M. *et al.* (2017) ‘Toward mountains without permanent snow and ice’, *Earth’s Future*, 5(5), pp. 418–435. Available at: <https://doi.org/10.1002/2016EF000514>.

Immerzeel, W.W. *et al.* (2010) ‘Climate Change Will Affect the Asian Water Towers’, *Science*, 328(5984), pp. 1382–1385. Available at: <https://doi.org/10.1126/science.1183188>.

Immerzeel, W.W. *et al.* (2014) ‘High-resolution monitoring of Himalayan glacier dynamics using unmanned aerial vehicles’, *Remote Sensing of Environment*, 150, pp. 93–103. Available at: <https://doi.org/10.1016/j.rse.2014.04.025>.

Immerzeel, W.W. *et al.* (2020) ‘Importance and vulnerability of the world’s water towers’, *Nature*, 577(7790), pp. 364–369. Available at: <https://doi.org/10.1038/s41586-019-1822-y>.

Kääb, A. *et al.* (2012) ‘Contrasting patterns of early twenty-first-century glacier mass change in the Himalayas’, *Nature*, 488(7412), pp. 495–498. Available at: <https://doi.org/10.1038/nature11324>.

Kayastha, R. *et al.* (2000) ‘Practical prediction of ice melting beneath various thickness of debris cover on Khumbu Glacier, Nepal, using a positive degree-day factor’, *IAHS-AISH Publication*, 264, pp. 71–81.

Kirkbride, M.P. and Deline, P. (2013) ‘The formation of supraglacial debris covers by primary dispersal from transverse englacial debris bands’, *Earth Surface Processes and Landforms*, 38(15), pp. 1779–1792. Available at: <https://doi.org/10.1002/esp.3416>.

Kraaijenbrink, P.D.A. *et al.* (2017) ‘Impact of a global temperature rise of 1.5 degrees Celsius on Asia’s glaciers’, *Nature*, 549(7671), pp. 257–260. Available at: <https://doi.org/10.1038/nature23878>.

- Kraaijenbrink, P.D.A. *et al.* (2018) ‘Mapping Surface Temperatures on a Debris-Covered Glacier With an Unmanned Aerial Vehicle’, *Frontiers in Earth Science*, 6. Available at: <https://doi.org/10.3389/feart.2018.00064>.
- Lalande, M. *et al.* (2021) ‘Climate change in the High Mountain Asia in CMIP6’, *Earth System Dynamics*, 12(4), pp. 1061–1098. Available at: <https://doi.org/10.5194/esd-12-1061-2021>.
- Lee, S.-I. (2017) ‘Correlation and Spatial Autocorrelation’, in S. Shekhar *et al.* (eds) *Encyclopedia of GIS*. Cham: Springer International Publishing, pp. 360–368. Available at: [https://doi.org/10.1007/978-3-319-17885-1\\_1524](https://doi.org/10.1007/978-3-319-17885-1_1524).
- Li, G. *et al.* (2018) ‘Heterogeneous decadal glacier downwasting at the Mt. Everest (Qomolangma) from 2000 to ~ 2012 based on multi-baseline bistatic SAR interferometry’, *Remote Sensing of Environment*, 206, pp. 336–349. Available at: <https://doi.org/10.1016/j.rse.2017.12.032>.
- Macfarlane, R. (2008) *Mountains of the Mind: A History of a Fascination*. Granta.
- Marzeion, B. *et al.* (2014) ‘Glaciers. Attribution of global glacier mass loss to anthropogenic and natural causes’, *Science (New York, N.Y.)*, 345(6199), pp. 919–921. Available at: <https://doi.org/10.1126/science.1254702>.
- Mattson, L. *et al.* (1993) ‘Ablation on debris covered glaciers : an example from the Rakhiot Glacier, Punjab, Himalaya’, *Snow and Glacier Hydrology* [Preprint]. Available at: <https://cir.nii.ac.jp/crid/1573950399945321472> (Accessed: 10 October 2024).
- Maurer, J.M. *et al.* (2019) ‘Acceleration of ice loss across the Himalayas over the past 40 years’, *Science Advances*, 5(6), p. eaav7266. Available at: <https://doi.org/10.1126/sciadv.aav7266>.
- McCarthy, M. *et al.* (2022) ‘Supraglacial debris thickness and supply rate in High-Mountain Asia’, *Communications Earth & Environment*, 3(1), pp. 1–11. Available at: <https://doi.org/10.1038/s43247-022-00588-2>.
- McCarthy, M.J. (2019) ‘Quantifying supraglacial debris thickness at local to regional scales’. Available at: <https://doi.org/10.17863/CAM.41172>.
- Mihalcea, C. *et al.* (2008a) ‘Spatial distribution of debris thickness and melting from remote-sensing and meteorological data, at debris-covered Baltoro glacier, Karakoram, Pakistan’, *Annals of Glaciology*, 48, pp. 49–57. Available at: <https://doi.org/10.3189/172756408784700680>.

- Mihalcea, C. *et al.* (2008b) ‘Using ASTER satellite and ground-based surface temperature measurements to derive supraglacial debris cover and thickness patterns on Miage Glacier (Mont Blanc Massif, Italy)’, *Cold Regions Science and Technology*, 52(3), pp. 341–354. Available at: <https://doi.org/10.1016/j.coldregions.2007.03.004>.
- Miles, K.E. *et al.* (2019) ‘Surface and subsurface hydrology of debris-covered Khumbu Glacier, Nepal, revealed by dye tracing’, *Earth and Planetary Science Letters*, 513, pp. 176–186. Available at: <https://doi.org/10.1016/j.epsl.2019.02.020>.
- Miles, K.E. *et al.* (2020) ‘Hydrology of debris-covered glaciers in High Mountain Asia’, *Earth-Science Reviews*, 207, p. 103212. Available at: <https://doi.org/10.1016/j.earscirev.2020.103212>.
- Miles, K.E. *et al.* (2021) ‘Continuous borehole optical televiewing reveals variable englacial debris concentrations at Khumbu Glacier, Nepal’, *Communications Earth & Environment*, 2(1), pp. 1–9. Available at: <https://doi.org/10.1038/s43247-020-00070-x>.
- Nicholson, L. and Benn, D.I. (2006) ‘Calculating ice melt beneath a debris layer using meteorological data’, *Journal of Glaciology*, 52(178), pp. 463–470. Available at: <https://doi.org/10.3189/172756506781828584>.
- Nicholson, L. and Benn, D.I. (2013) ‘Properties of natural supraglacial debris in relation to modelling sub-debris ice ablation’, *Earth Surface Processes and Landforms*, 38(5), pp. 490–501. Available at: <https://doi.org/10.1002/esp.3299>.
- Nicholson, L. and Mertes, J. (2017) ‘Thickness estimation of supraglacial debris above ice cliff exposures using a high-resolution digital surface model derived from terrestrial photography’, *Journal of Glaciology*, 63(242), pp. 989–998. Available at: <https://doi.org/10.1017/jog.2017.68>.
- Nuth, C. and Kääb, A. (2011) ‘Co-registration and bias corrections of satellite elevation data sets for quantifying glacier thickness change’, *The Cryosphere*, 5(1), pp. 271–290. Available at: <https://doi.org/10.5194/tc-5-271-2011>.
- Østrem, G. (1959) ‘Ice Melting under a Thin Layer of Moraine, and the Existence of Ice Cores in Moraine Ridges’, *Geografiska Annaler*, 41(4), pp. 228–230. Available at: <https://doi.org/10.1080/20014422.1959.11907953>.
- Paul, F. *et al.* (2004) ‘Combining satellite multispectral image data and a digital elevation model for mapping debris-covered glaciers’, *Remote Sensing of Environment*, 89(4), pp. 510–518. Available at: <https://doi.org/10.1016/j.rse.2003.11.007>.

- Pfeffer, W.T. *et al.* (2014) ‘The Randolph Glacier Inventory: a globally complete inventory of glaciers’, *Journal of Glaciology*, 60(221), pp. 537–552. Available at: <https://doi.org/10.3189/2014JoG13J176>.
- Quincey, D.J. *et al.* (2009) ‘Quantification of Everest region glacier velocities between 1992 and 2002, using satellite radar interferometry and feature tracking’, *Journal of Glaciology*, 55(192), pp. 596–606.
- Ragettli, S. *et al.* (2015) ‘Unraveling the hydrology of a Himalayan catchment through integration of high resolution in situ data and remote sensing with an advanced simulation model’, *Advances in Water Resources*, 78, pp. 94–111. Available at: <https://doi.org/10.1016/j.advwatres.2015.01.013>.
- Reid, T.D. and Brock, B.W. (2010) ‘An energy-balance model for debris-covered glaciers including heat conduction through the debris layer’, *Journal of Glaciology*, 56(199), pp. 903–916. Available at: <https://doi.org/10.3189/002214310794457218>.
- Reznichenko, N.V. *et al.* (2011) ‘Effects of rock avalanches on glacier behaviour and moraine formation’, *Geomorphology*, 132(3), pp. 327–338. Available at: <https://doi.org/10.1016/j.geomorph.2011.05.019>.
- RGI Consortium (2023) ‘Randolph Glacier Inventory - A Dataset of Global Glacier Outlines, Version 7’. Available at: <https://doi.org/10.5067/F6JMOVY5NAVZ>.
- Rounce, D.R. *et al.* (2015) ‘Debris-covered glacier energy balance model for Imja–Lhotse Shar Glacier in the Everest region of Nepal’, *The Cryosphere*, 9(6), pp. 2295–2310. Available at: <https://doi.org/10.5194/tc-9-2295-2015>.
- Rounce, D.R. *et al.* (2018) ‘Quantifying Debris Thickness of Debris-Covered Glaciers in the Everest Region of Nepal Through Inversion of a Subdebris Melt Model’, *Journal of Geophysical Research: Earth Surface*, 123(5), pp. 1094–1115. Available at: <https://doi.org/10.1029/2017JF004395>.
- Rounce, D.R. *et al.* (2021) ‘Distributed Global Debris Thickness Estimates Reveal Debris Significantly Impacts Glacier Mass Balance’, *Geophysical Research Letters*, 48(8), p. e2020GL091311. Available at: <https://doi.org/10.1029/2020GL091311>.
- Rounce, D.R. and McKinney, D.C. (2014) ‘Debris thickness of glaciers in the Everest area (Nepal Himalaya) derived from satellite imagery using a nonlinear energy balance model’, *The Cryosphere*, 8(4), pp. 1317–1329. Available at: <https://doi.org/10.5194/tc-8-1317-2014>.
- Rowan, A.V. *et al.* (2015) ‘Modelling the feedbacks between mass balance, ice flow and debris transport to predict the response to climate change of debris-covered glaciers in the

- Himalaya', *Earth and Planetary Science Letters*, 430, pp. 427–438. Available at: <https://doi.org/10.1016/j.epsl.2015.09.004>.
- Sakai, A. and Fujita, K. (2017) 'Contrasting glacier responses to recent climate change in high-mountain Asia', *Scientific Reports*, 7(1), p. 13717. Available at: <https://doi.org/10.1038/s41598-017-14256-5>.
- Salerno, F. et al. (2017) 'Debris-covered glacier anomaly? Morphological factors controlling changes in the mass balance, surface area, terminus position, and snow line altitude of Himalayan glaciers', *Earth and Planetary Science Letters*, 471, pp. 19–31. Available at: <https://doi.org/10.1016/j.epsl.2017.04.039>.
- Scaramuzza, P. and Barsi, J. (2005) 'Landsat 7 scan line corrector-off gap-filled product development', in *Proceeding of Pecora*, pp. 23–27.
- Schauwecker, S. et al. (2015) 'Remotely sensed debris thickness mapping of Bara Shigri Glacier, Indian Himalaya', *Journal of Glaciology*, 61(228), pp. 675–688. Available at: <https://doi.org/10.3189/2015JoG14J102>.
- Scherler, D. et al. (2011) 'Spatially variable response of Himalayan glaciers to climate change affected by debris cover', *Nature Geoscience*, 4(3), pp. 156–159. Available at: <https://doi.org/10.1038/ngeo1068>.
- Scherler, D. et al. (2018) 'Global Assessment of Supraglacial Debris-Cover Extents', *Geophysical Research Letters*, 45(21). Available at: <https://doi.org/10.1029/2018GL080158>.
- Shea, J.M. et al. (2021) 'Debris Emergence Elevations and Glacier Change', *Frontiers in Earth Science*, 9. Available at: <https://doi.org/10.3389/feart.2021.709957>.
- Shean, D.E. et al. (2020) 'A Systematic, Regional Assessment of High Mountain Asia Glacier Mass Balance', *Frontiers in Earth Science*, 7. Available at: <https://doi.org/10.3389/feart.2019.00363>.
- Shen, Z. (1975) 'Air temperature and its change with altitude at the northern slope of Mt. Qomolangma', in T.S.E.T. o C.A. o Sciences (ed.) *Meteorology and solar radiation in report of Scientific Expedition in the Mt. Qomolangma Region (1966-1968)*. Beijing, pp. 4–10.
- Shrestha, F. et al. (2023) 'A comprehensive and version-controlled database of glacial lake outburst floods in High Mountain Asia', *Earth System Science Data*, 15(9), pp. 3941–3961. Available at: <https://doi.org/10.5194/essd-15-3941-2023>.

- Steiner, J.F. and Pellicciotti, F. (2016) ‘Variability of air temperature over a debris-covered glacier in the Nepalese Himalaya’, *Annals of Glaciology*, 57(71), pp. 295–307. Available at: <https://doi.org/10.3189/2016AoG71A066>.
- Stewart, R.L. *et al.* (2021) ‘Using climate reanalysis data in conjunction with multi-temporal satellite thermal imagery to derive supraglacial debris thickness changes from energy-balance modelling’, *Journal of Glaciology*, 67(262), pp. 366–384. Available at: <https://doi.org/10.1017/jog.2020.111>.
- Taylor, J.R. (1997) *An Introduction to Error Analysis: The Study of Uncertainties in Physical Measurements*. University Science Books (ASMSU/Spartans.4.Spartans Textbook). Available at: <https://books.google.co.uk/books?id=ypNnQgAACAAJ>.
- Thakuri, S. *et al.* (2014) ‘Tracing glacier changes since the 1960s on the south slope of Mt. Everest (central Southern Himalaya) using optical satellite imagery’, *The Cryosphere*, 8(4), pp. 1297–1315. Available at: <https://doi.org/10.5194/tc-8-1297-2014>.
- Velasco, V.M. *et al.* (2024) *Inferring Debris Properties on Debris-Covered Glaciers: Implications for Glacier Modelling*. EGU24-9702. Copernicus Meetings. Available at: <https://doi.org/10.5194/egusphere-egu24-9702>.
- Watson, C.S. *et al.* (2016) ‘The dynamics of supraglacial ponds in the Everest region, central Himalaya’, *Global and Planetary Change*, 142, pp. 14–27. Available at: <https://doi.org/10.1016/j.gloplacha.2016.04.008>.
- Wessels, R.L. *et al.* (2002) ‘ASTER measurement of supraglacial lakes in the Mount Everest region of the Himalaya’, *Annals of Glaciology*, 34, pp. 399–408. Available at: <https://doi.org/10.3189/172756402781817545>.
- Westoby, M.J. *et al.* (2020) ‘Geomorphological evolution of a debris-covered glacier surface’, *Earth Surface Processes and Landforms*, 45(14), pp. 3431–3448. Available at: <https://doi.org/10.1002/esp.4973>.
- Ye, Q. *et al.* (2009) ‘Monitoring Glacier and Supra-glacier Lakes from Space in Mt. Qomolangma Region of the Himalayas on the Tibetan Plateau in China’, *Journal of Mountain Science*, 6, pp. 211–220. Available at: <https://doi.org/10.1007/s11629-009-1016-4>.
- Ye, Q. *et al.* (2015) ‘Glacier mass changes in Rongbuk catchment on Mt. Qomolangma from 1974 to 2006 based on topographic maps and ALOS PRISM data’, *Journal of Hydrology*, 530, pp. 273–280. Available at: <https://doi.org/10.1016/j.jhydrol.2015.09.014>.

Ye, Q. *et al.* (2022) ‘Monitoring glacier thinning rate in Rongbuk Catchment on the northern slope of Mt. Qomolangma from 1974 to 2021’, *Ecological Indicators*, 144, p. 109418. Available at: <https://doi.org/10.1016/j.ecolind.2022.109418>.

Zemp, M. *et al.* (2019) ‘Global glacier mass changes and their contributions to sea-level rise from 1961 to 2016’, *Nature*, 568(7752), pp. 382–386. Available at: <https://doi.org/10.1038/s41586-019-1071-0>.

Zhao, L. *et al.* (2016) ‘The High Mountain Asia glacier contribution to sea-level rise from 2000 to 2050’, *Annals of Glaciology*, 57(71), pp. 223–231. Available at: <https://doi.org/10.3189/2016AoG71A049>.

Zheng, G. *et al.* (2021) ‘Increasing risk of glacial lake outburst floods from future Third Pole deglaciation’, *Nature Climate Change*, 11(5), pp. 411–417. Available at: <https://doi.org/10.1038/s41558-021-01028-3>.

## 8 Appendices

### 8.1 Appendix 1 - Landsat 7 ETM+ image codes

---

Landsat 7 Acquisition Date	Landsat 7 Image Code(s)
12/09/2000	LANDSAT/LE07/C02/T1_L2/LE07_140040_20000912, LANDSAT/LE07/C02/T1_L2/LE07_140041_20000912
15/09/2001	LANDSAT/LE07/C02/T1_L2/LE07_140041_20010915
14/06/2002	LANDSAT/LE07/C02/T1_L2/LE07_140041_20020614
16/05/2003	LANDSAT/LE07/C02/T1_L2/LE07_140040_20030516, LANDSAT/LE07/C02/T1_L2/LE07_140041_20030516
03/06/2004	LANDSAT/LE07/C02/T1_L2/LE07_140040_20040603, LANDSAT/LE07/C02/T1_L2/LE07_140041_20040603
22/08/2004	LANDSAT/LE07/C02/T1_L2/LE07_140040_20040822, LANDSAT/LE07/C02/T1_L2/LE07_140041_20040822
07/09/2004	LANDSAT/LE07/C02/T1_L2/LE07_140040_20040907, LANDSAT/LE07/C02/T1_L2/LE07_140041_20040907
06/06/2005	LANDSAT/LE07/C02/T1_L2/LE07_140040_20050606, LANDSAT/LE07/C02/T1_L2/LE07_140041_20050606
09/06/2006	LANDSAT/LE07/C02/T1_L2/LE07_140040_20060609, LANDSAT/LE07/C02/T1_L2/LE07_140041_20060609
27/05/2007	LANDSAT/LE07/C02/T1_L2/LE07_140040_20070527, LANDSAT/LE07/C02/T1_L2/LE07_140041_20070527
12/06/2007	LANDSAT/LE07/C02/T1_L2/LE07_140040_20070612, LANDSAT/LE07/C02/T1_L2/LE07_140041_20070612
29/05/2008	LANDSAT/LE07/C02/T1_L2/LE07_140040_20080529, LANDSAT/LE07/C02/T1_L2/LE07_140041_20080529
02/09/2008	LANDSAT/LE07/C02/T1_L2/LE07_140040_20080902, LANDSAT/LE07/C02/T1_L2/LE07_140041_20080902
17/06/2009	LANDSAT/LE07/C02/T1_L2/LE07_140040_20090617, LANDSAT/LE07/C02/T1_L2/LE07_140041_20090617
22/05/2011	LANDSAT/LE07/C02/T1_L2/LE07_140040_20110522, LANDSAT/LE07/C02/T1_L2/LE07_140041_20110522
24/05/2012	LANDSAT/LE07/C02/T1_L2/LE07_140040_20120524, LANDSAT/LE07/C02/T1_L2/LE07_140041_20120524
09/06/2012	LANDSAT/LE07/C02/T1_L2/LE07_140040_20120609, LANDSAT/LE07/C02/T1_L2/LE07_140041_20120609

11/07/2012	LANDSAT/LE07/C02/T1_L2/LE07_140040_20120711, LANDSAT/LE07/C02/T1_L2/LE07_140041_20120711
16/09/2013	LANDSAT/LE07/C02/T1_L2/LE07_140040_20130916, LANDSAT/LE07/C02/T1_L2/LE07_140041_20130916
03/09/2014	LANDSAT/LE07/C02/T1_L2/LE07_140040_20140903, LANDSAT/LE07/C02/T1_L2/LE07_140041_20140903
06/09/2015	LANDSAT/LE07/C02/T1_L2/LE07_140040_20150906, LANDSAT/LE07/C02/T1_L2/LE07_140041_20150906
19/05/2016	LANDSAT/LE07/C02/T1_L2/LE07_140040_20160519, LANDSAT/LE07/C02/T1_L2/LE07_140041_20160519
07/08/2016	LANDSAT/LE07/C02/T1_L2/LE07_140040_20160807, LANDSAT/LE07/C02/T1_L2/LE07_140041_20160807
23/08/2016	LANDSAT/LE07/C02/T1_L2/LE07_140040_20160823, LANDSAT/LE07/C02/T1_L2/LE07_140041_20160823
23/06/2017	LANDSAT/LE07/C02/T1_L2/LE07_140040_20170623, LANDSAT/LE07/C02/T1_L2/LE07_140041_20170623
11/09/2017	LANDSAT/LE07/C02/T1_L2/LE07_140040_20170911, LANDSAT/LE07/C02/T1_L2/LE07_140041_20170911
10/06/2018	LANDSAT/LE07/C02/T1_L2/LE07_140040_20180610, LANDSAT/LE07/C02/T1_L2/LE07_140041_20180610
28/07/2018	LANDSAT/LE07/C02/T1_L2/LE07_140040_20180728, LANDSAT/LE07/C02/T1_L2/LE07_140041_20180728
28/05/2019	LANDSAT/LE07/C02/T1_L2/LE07_140040_20190528, LANDSAT/LE07/C02/T1_L2/LE07_140041_20190528
13/06/2019	LANDSAT/LE07/C02/T1_L2/LE07_140040_20190613, LANDSAT/LE07/C02/T1_L2/LE07_140041_20190613
29/06/2019	LANDSAT/LE07/C02/T1_L2/LE07_140040_20190629, LANDSAT/LE07/C02/T1_L2/LE07_140041_20190629
31/07/2019	LANDSAT/LE07/C02/T1_L2/LE07_140040_20190731, LANDSAT/LE07/C02/T1_L2/LE07_140041_20190731
01/07/2020	LANDSAT/LE07/C02/T1_L2/LE07_140040_20200701, LANDSAT/LE07/C02/T1_L2/LE07_140041_20200701
02/08/2020	LANDSAT/LE07/C02/T1_L2/LE07_140040_20200802, LANDSAT/LE07/C02/T1_L2/LE07_140041_20200802
18/08/2020	LANDSAT/LE07/C02/T1_L2/LE07_140040_20200818, LANDSAT/LE07/C02/T1_L2/LE07_140041_20200818
04/07/2021	LANDSAT/LE07/C02/T1_L2/LE07_140040_20210704, LANDSAT/LE07/C02/T1_L2/LE07_140041_20210704

## 8.2 Appendix 2 - ERA-5 data

Landsat 7 Acquisition Date	Nearest ERA- 2m Air Temperature (K)	Solar Downwards Thermal Downwards (W m <sup>-2</sup> )	Specific Humidity (g kg <sup>-1</sup> )	Humidity (%)	Wind Speed (m s <sup>-1</sup> )	Sun Elevation (°)	Sun Azimuth (°)
12/09/2000	5.00	278.91	823.05	241.42	6.51	78.19	2.155
15/09/2001	5.00	278.67	905.67	236.01	6.57	79.77	1.941
14/06/2002	5.00	278.43	836.79	261.41	6.85	83.20	2.358
16/05/2003	5.00	271.88	952.31	221.48	5.86	88.67	2.231
03/06/2004	5.00	275.36	830.93	265.15	6.33	85.21	2.402
22/08/2004	5.00	280.53	873.44	266.17	6.95	79.17	2.348
07/09/2004	5.00	281.34	673.91	273.07	7.20	79.88	1.255
06/06/2005	5.00	275.05	977.59	232.02	6.02	81.96	2.233
09/06/2006	5.00	278.68	837.32	283.05	7.10	85.57	1.916
27/05/2007	5.00	275.98	985.55	220.88	6.23	82.49	2.838
12/06/2007	5.00	280.42	963.79	245.29	6.78	77.21	0.648
29/05/2008	5.00	275.23	994.44	236.78	6.51	88.01	2.217
02/09/2008	5.00	277.78	713.94	281.53	6.96	86.84	1.949
17/06/2009	5.00	278.55	909.86	248.42	7.24	87.76	2.228
22/05/2011	5.00	273.99	823.91	256.11	6.69	94.19	1.856
24/05/2012	5.00	276.64	1013.26	220.11	5.55	71.51	1.072
09/06/2012	5.00	277.21	899.09	244.67	7.14	90.21	2.193
11/07/2012	5.00	278.79	823.04	264.93	7.37	88.84	1.653
16/09/2013	5.00	276.46	705.81	270.14	6.59	85.65	2.342
03/09/2014	5.00	279.62	918.09	255.59	6.83	80.26	1.596
06/09/2015	5.00	279.18	656.23	289.20	7.63	91.00	2.013
19/05/2016	5.00	274.82	978.47	224.01	6.01	82.68	2.230
07/08/2016	5.00	280.43	764.93	297.32	8.27	94.37	1.633
23/08/2016	5.00	279.31	791.56	275.53	7.14	84.86	1.235
23/06/2017	5.00	278.03	910.98	270.48	6.86	84.59	2.027
11/09/2017	5.00	278.75	772.82	268.42	6.63	80.29	2.025
10/06/2018	5.00	277.02	757.40	282.94	7.18	91.34	1.459
28/07/2018	5.00	279.88	768.92	303.47	7.57	87.77	1.398
28/05/2019	5.00	273.85	951.71	227.10	6.21	88.23	1.926
13/06/2019	5.00	278.08	957.92	242.88	6.89	84.89	1.137
29/06/2019	5.00	278.60	710.65	289.18	7.30	88.17	2.051
31/07/2019	5.00	279.37	694.06	301.14	7.49	88.53	1.717
01/07/2020	4.00	277.80	631.91	274.01	7.49	92.12	1.438
02/08/2020	4.00	277.55	352.32	313.91	7.40	91.78	0.667
18/08/2020	4.00	280.56	828.06	235.74	5.84	65.55	1.852
04/07/2021	4.00	278.21	627.69	296.40	7.37	89.50	2.097

### 8.3 Appendix 3 –Effective geographical sample size

Section 3.3 introduced Equation (8), derived from Grace (2019):

$$\sigma_{\text{Adj}} = \sigma \sqrt{\left(\frac{1+I}{1-I}\right)},$$

to adjust the uncertainty in derived results to account for spatial autocorrelation in uncertainties when, for example, calculating the total volume of debris change. Spatial autocorrelation means that uncertainties are less likely to cancel, meaning quadrature-derived uncertainties (which assume independence) are likely to underestimate the true uncertainty (Taylor, 1997; Griffith, 2005; Lee, 2017).

This section explains Equation (8)'s derivation.

The effective sample size represents the equivalent number of independent observations needed to provide the same uncertainty as those that are correlated (Griffith, 2005; Grace, 2019). From Grace (2019), the effective *geographical* sample size can be calculated using a Moran's I test:

$$N_{\text{Eff}} = N \left( \frac{1-I}{I+1} \right), \quad (10)$$

where  $I$  is Moran's I value, calculated from a Moran's I test on the distributed debris thickness uncertainty map, and  $N$  is the sample size.

The adjusted uncertainty is:

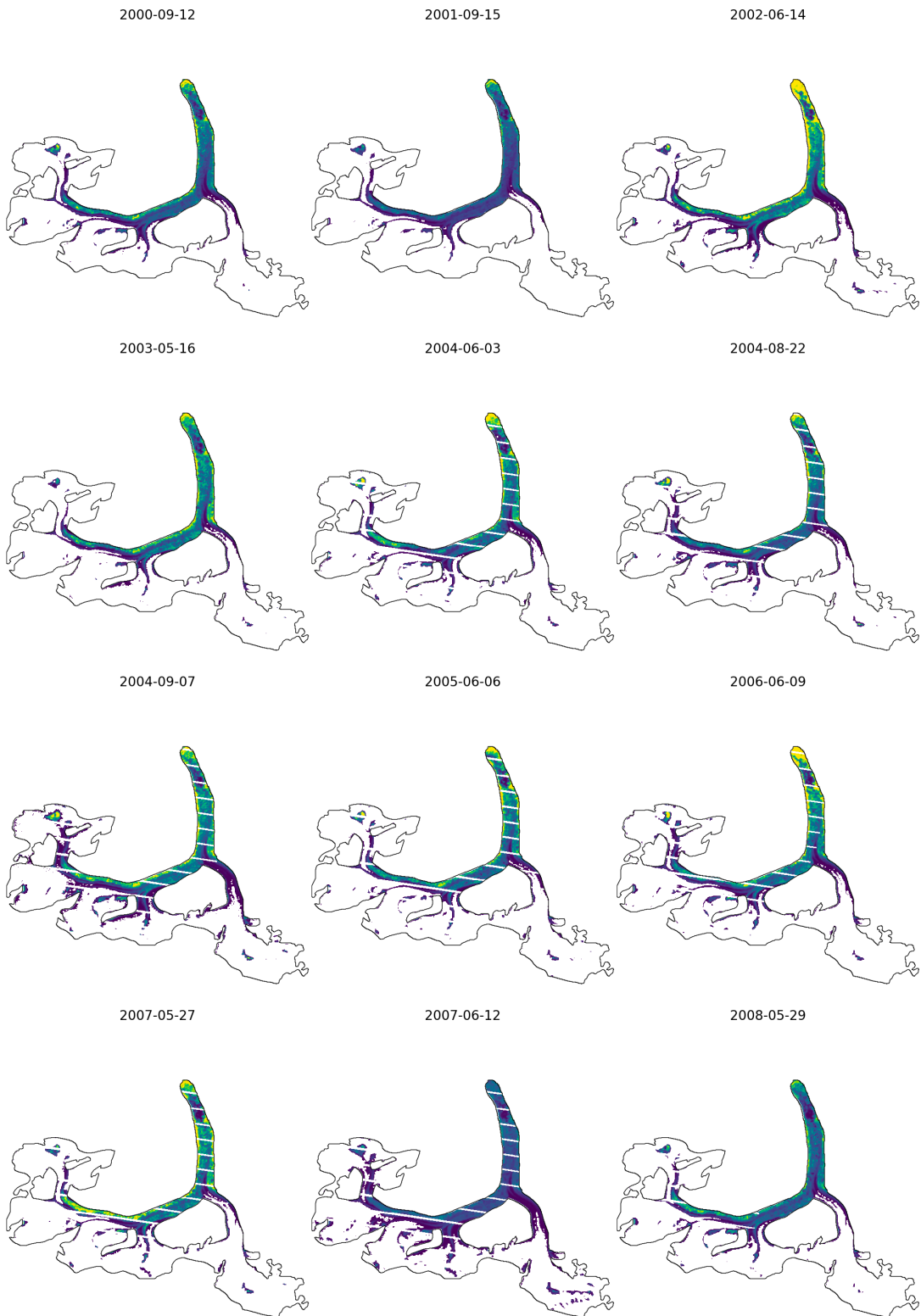
$$\sigma_{\text{Adj}} = \sigma \sqrt{\frac{N}{N_{\text{Eff}}}}. \quad (11)$$

Substituting (10) into (11) results in  $N$  cancelling, thereby providing Equation (8):

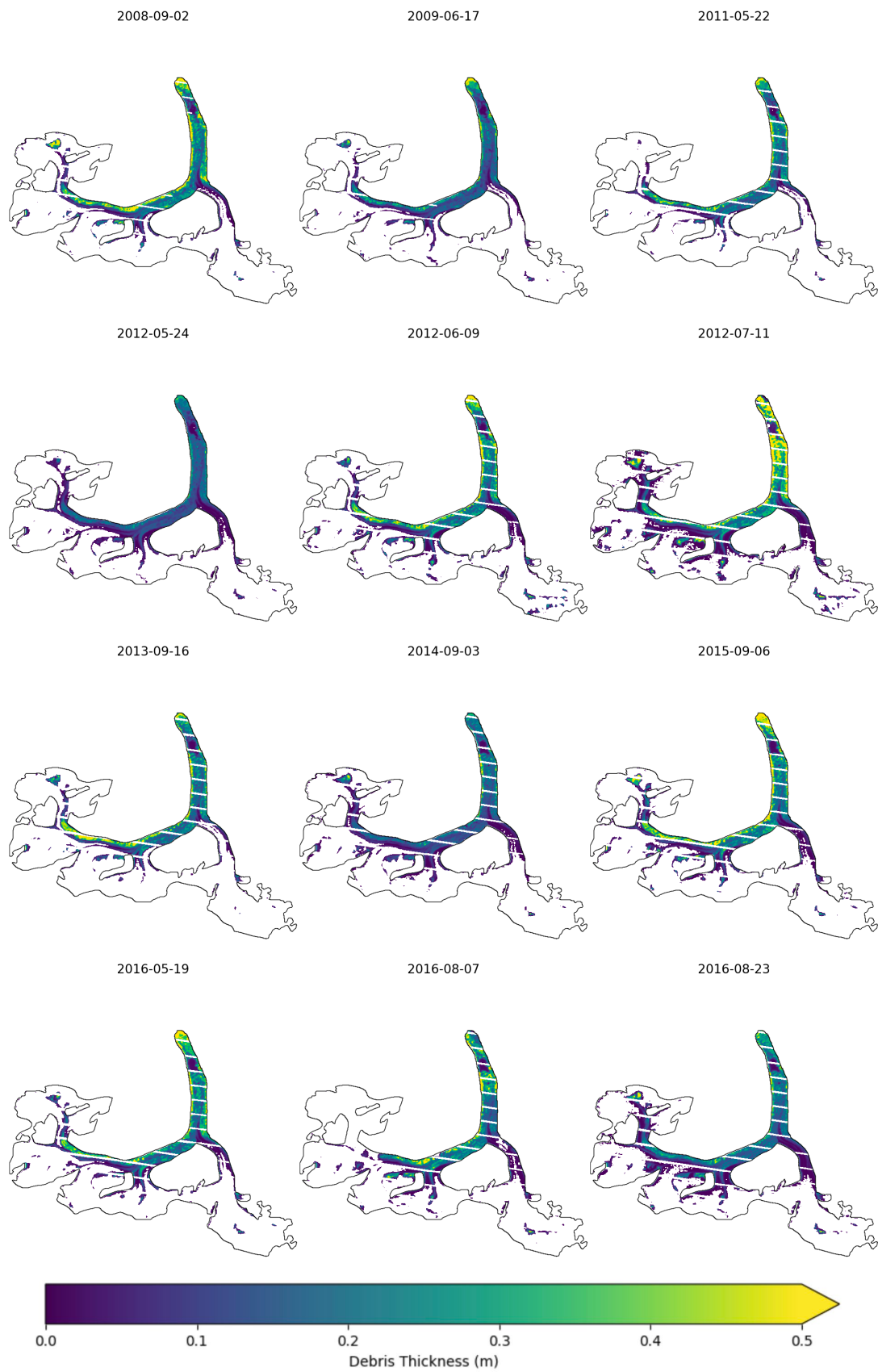
$$\sigma_{\text{Adj}} = \sigma \sqrt{\left(\frac{1+I}{1-I}\right)}.$$

Note the reciprocal of the fraction in (10), owing to it being on the denominator in (11).

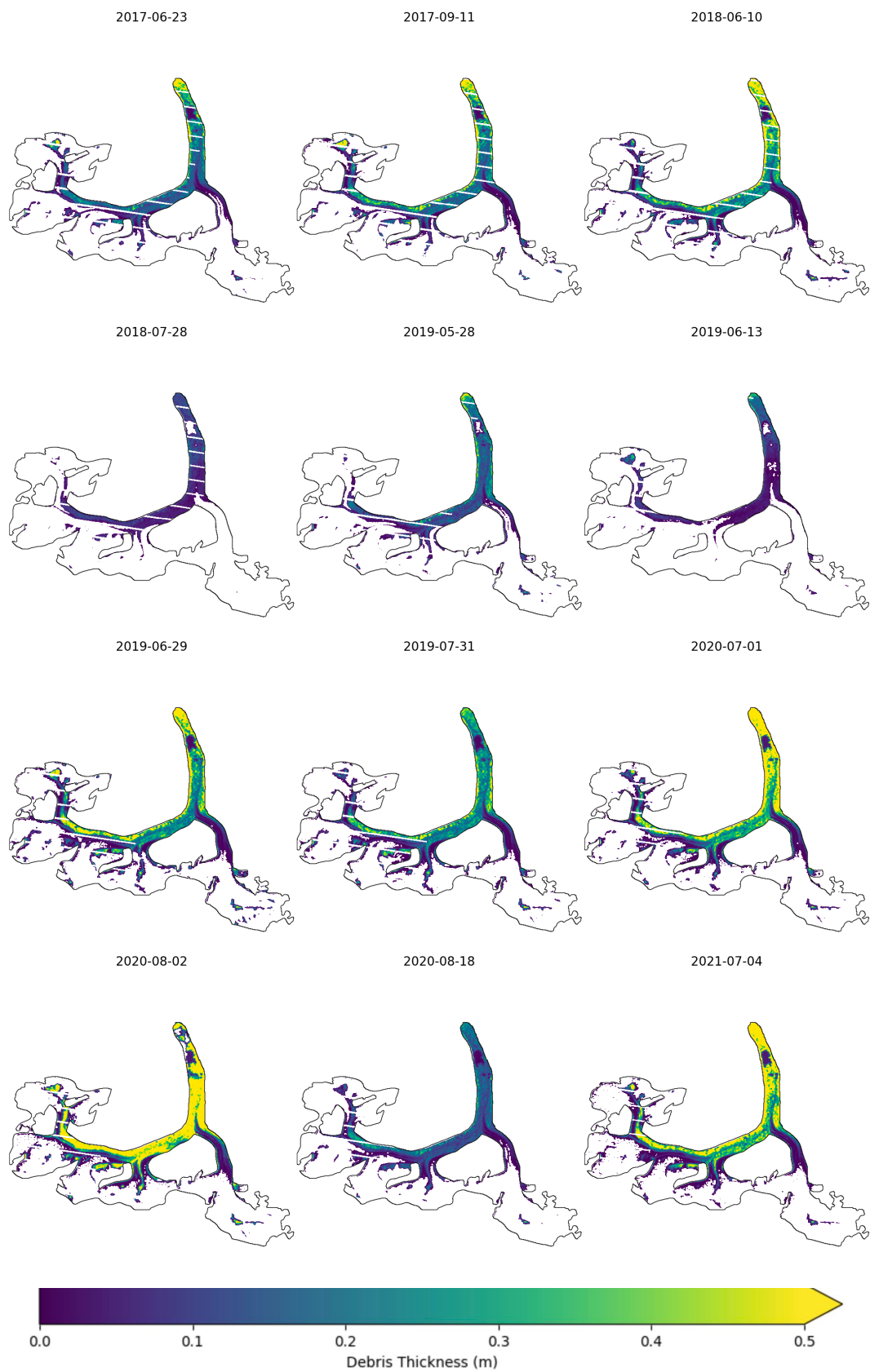
## 8.4 Appendix 4 – Distributed debris thickness maps



376\_7084A\_DISS\_2025



# 376\_7084A\_DISS\_2025



## 8.5 Appendix 5 – Stacked and averaged distributed debris thickness maps

